BACHELOR THESIS

Modeling the Influence of Gas Expansion on the Linear Response of Laminar Premixed Flames

Autor:
Axel Zimmermann

Matrikel-No:
03670624

Betreuer:
Prof. Wolfgang Polifke, Ph. D.
Thomas Steinbacher, Dipl. Ing.

October 16, 2018

Technische Universität München
Fakultät für Maschinenwesen
Professur für Thermofluiddynamik
Prof. Wolfgang Polifke, Ph. D.

Erklärung

Hiermit versichere ich, die vorliegende Arbeit selbstständig verfasst zu haben. Ich habe keine anderen Quellen und Hilfsmittel als die angegebenen verwendet.

Ort, Datum	Axel Zimmermann

Abstract

Thermoacoustic oscillations, arising due to the interaction of the flame front and the acoustics of the system, can reduce the life span of combustion systems. To counteract any undesirable qualities, an in-depth knowledge of the dominating processes is required. Therefore often low order models are applied. A low order model describing the flame motion is the G-equation. For the G-equation, an accurate velocity model is needed. Such a velocity model is derived in this thesis. This model can capture the impact of the flame front induced gas expansion on the velocity field. Therefore, several modified sources are positioned on the flame front. It is found that the velocity profile obtained by this model is well aligned with the velocity profile of Cantera simulations for an unstretched flame front. However, a big advantage of this model is that it needs little computational cost. In combination with a G-equation solver, the impact of the gas expansion on the linear response of premixed flames is investigated. It is found that the gas expansion increases the flame shape curvature. In addition to that, the gas expansion alters the linear response of the flame towards an acoustic excitation. It leads to an oscillating impulse response accompanied with a high magnitude in frequency response at that oscillation frequency. It is also found that the gas expansion has to be accounted for the existence of convective waves in the upstream flow of an perturbed flame front and the Darrius-Landau mechanism.

Contents

Nomenclature

Acronyms

CFD	Computational Fluid Dynamics
CID	Convective Incompressible with Dirac Kernel
CIG	Convective Incompressible with Gaussian Kernel
FFD	Flame Foot Displacement
FR	Frequency Response
FTF	Flame Transfer Function
IR	Impulse Response
SDF	Signed Distance Function

Functions and Mathematical Operators

$\mathcal{O}(\cdot)$	Order of Magnitude
$*$	Temporal Convolution
$\delta(t)$	Dirac Function
$\frac{D\cdot}{Dt}$	Substantial Derivative after the Time
∇	Nabla Operator
$\frac{\partial\cdot}{\partial a}$	Partial Derivative after the Parameter a
$exp(\cdot)$	Exponential Function
$F(\omega)$	Frequency Response Function
$h(t)$	Impulse Response Function
i	Imaginary Number

$sgn(\cdot)$	Sign Function	

Greek Symbols

α	Angle between Flame and Horizontal Line	[rad]
β	Angle of Kutta-Panel	[rad]
δ_f	Flame Thickness	[m]
Δ_g	Gap	[m]
δ_M	Markstein Length	[m]
Δ_o	Overlap	[m]
η	Horizontal Flame Coordinate	[m]
κ	Flame Stretching Rate	[1/m]
κ_{Curv}	Curvature	[1/m]
κ_s	Strain Related Stretch	[1/m]
ω	Circular Frequency	[1/s]
Φ	Potential / Equivalence Ratio	
ρ	Density	[kg/m^3]
σ	Kernel Width	[m]
σ_g	Growth Rate	[1/s]
τ	Pseudo Time Step	[-]
τ_c	Convective Time Scale	[s]
τ_r	Time of Restoration	[s]
$\vec{\Omega}$	Vorticity Vector	[1/s]
ξ	Complex Coordinate in Image Domain / Perturbation	[m]

Roman Symbols

Δh_R	Heat of Reaction	[J/kg]
Δ_s	Length of the Flame Front Part	[m]
$\dot{Q}$	Heat Flux	[J/s]

$\dot{V}_E$	Entering Volume Flux	$[\mathrm{m}^3/\mathrm{s}]$
$\dot{V}_l$	Leaving Volume Flux	$[\mathrm{m}^3/\mathrm{s}]$
$\dot{V}_p$	Produced Volume Flux	$[\mathrm{m}^3/\mathrm{s}]$
$\vec{n}$	Normal Vector	[m]
$\vec{u}$	Velocity Vector $[u_1, u_2]$	[m/s]
$\vec{v}_F$	Absolute Flame Velocity	[m/s]
$\vec{x}$	Space Vector $[x_1, x_2]$	[m]
A	Flame Front Surface	$[\mathrm{m}^2]$
a_Ψ	Radius of Curvature of a Streamline	[m]
C_r	Confinement Ratio	[-]
D	Duct Diameter	[m]
E	Expansion Ratio	[-]
f	Frequency	[1/s]
f_b	Parameter for FBD-Model	[m/s]
G	G-Field	
H	Length of Kutta-Panel	[m]
He	Helmholtz Number	[-]
K	Parameter for the CIG-Model	[-]
k	Wavenumber	[1/m]
k_{crit}	Critical Wavenumber	[1/m]
L_F	Flame Length	[m]
M	Mach Number	[-]
N	Number of Sources	[-]
p	Pressure	[Pa]
r	Radial Coordinate	[m]
r_0	Source Radius	[m]

R_a	Combustor Radius	[m]
R_i	Feed Channel Radius	[m]
s_L^0	Unstretched Laminar Burning Velocity	[m/s]
s_Ψ	Coordinate along a Streamline	[m]
s_L	Laminar Burning Velocity	[m/s]
t	Time	[s]
T_b	Burnt Temperature	[K]
T_R	Reaction Temperature	[K]
T_u	Unburnt Temperature	[K]
u	Absolute Velocity / Complex Velocity	[m/s]
u'_E	Excitation Velocity	[m/s]
u'_{ac}	Acoustic Velocity	[m/s]
u_c	Convective Velocity	[m/s]
u_E	Entering Velocity	[m/s]
u_r	Restoration Velocity /Radial Velocity	[m/s]
u_{bulk}	Bulk Flow Velocity	[m/s]
u_{pot}	Potential Velocity	[m/s]
u_{ref}	Reference Velocity	[m/s]
x	Complex Coordinate	[m]
x^F	Flame Aligned Coordinate System	[m]
x^L	Laboratory Aligned Coordinate System	[m]
Le	Lewis Number	[-]
Ma	Markstein Number	[-]

Superscripts and Subscripts

$(\cdot)'$	Fluctuating Parameter
$(\cdot)^*$	Non-Dimensional Parameter

$(\cdot)_\parallel$	Parallel Parameter to the Flame Front
$(\cdot)_\perp$	Perpendicular Parameter to the Flame Front
$(\cdot)_\xi$	Parameter in Image Domain
$(\cdot)_b$	Burnt Parameter
$(\cdot)_r$	Radial Direction
$(\cdot)_s$	Induces Effect by a Source
$(\cdot)_u$	Unburnt Parameter
$(\bar{\cdot})$	Averaged Value
$(\tilde{\cdot})$	Complex Conjugate Parameter

1 Introduction

In times of global warming it is necessary to reduce the consumption of fossil fuels, which produce toxic gases like NO_x when burned with an oxidizer in engines or power plants. Therefore, especially premixed flames got in the center of interest. The advantage of premixing the gas mixture before burning it is that a lean combustion can be achieved and thus lower burning temperatures [13]. The lower the burning temperature, the less nitrogen oxides are produced and the thermal stress on the combustion system is decreased.
The problem about the premixed combustion technology is the sensitivity towards thermoacoustic-oscillations [13]. Those oscillations arise due to the interaction between the acoustics of the system and the combustion. The acoustics lead to velocity fluctuations u', which affect the flame front so that more or less heat $\dot{Q}$ is emanated by flame. This heat release fluctuation $\dot{Q}'$ then influences the acoustics of the system once again [15], see Figure 1.1. The feedback loop between the acoustics and the flame can become unstable, leading to high pressure waves [15]. Those pressure waves can cause mechanical damage and reduce the lifespan of the entire combustion system.
To control the thermoacoustic-instabilities, an in-depth understanding of the connection between the acoustic velocity fluctuation and the heat release fluctuation is required. In terms of linear analysis, both are connected by the flame transfer function (FTF). The FTF can either be analyzed in the time domain as the impulse response or in the frequency domain as the frequency response. Several analytic models have been developed predicting the FTF , see e.g. Fleifil et al. [12] or Schuller et al. [22]. The most successful models are the so called convective velocity models. Those models are based on experimental observations for acousticcaly excited flames. It was observed that convective waves arise in the upstream fluid traveling with the bulk flow speed [2]. Those waves dominate the motion of the unburnt gas, especially in the range of low frequencies [2]. Steinbacher et al. [26] demonstrated, that only the potential part of the acoustic velocity perurbation has to be considered for the FTF. However, the potential acoustic velocity field is not the reason for the convective waves. The high magnitude of the frequency response at certain excitation frequencies cannot be explained by the acoustic velocity perurbation alone. Hence, they concluded that the flame-flow feedback is very important for the FTF. In general, the flame-flow feedback constists of two mechanisms, barocline vorticity production and gas expansion. Blanchard et al. [3] modeled the effect of barocline vorticity in combination with a G-equation solver. They showed that the barocline vorticity can be accounted by the convective waves, but did not investigate the effect on the flame transfer function with the G-equation solver. Schlimpert et al. [21] investigated the effect of gas expansion by solving the compressible conservation equations for the fluid. They showed that the effect of gas expansion cannot be neglected when modeling the FTF.

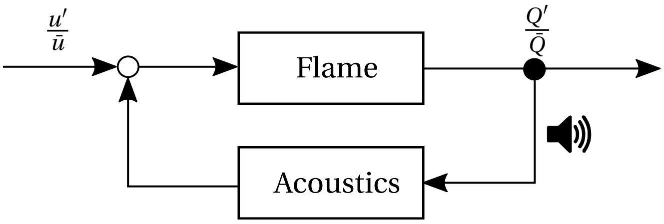

Figure 1.1: Schematic representation of the feedback-loop, consisting of the flame and the acoustics.

In this thesis, the effect of gas expansion on the FTF is investigated with a G-equation solver from Steinbacher [24]. Therefore, a velocity field u is modeled. This velocity field is decomposed as follows:

$$u = u_{bulk} + u'_{ac} + u_{vol} \tag{1.1}$$

Here, u_{bulk}, u'_{ac} and u_{vol} denote the potential bulk flow without flame-flow feedback, the potential aoustic velocity field and the gas expansion induced velocity field, respectively. The apostrophe at u'_{ac} indicates that the acoustic velocity field is small compared to u_{bulk} and u_{vol}. For u_{vol}, a new model is derived, based on modified sources. This model is restricted to a two dimensional inviscid and incompressible flow.

Before the new model is derived, a brief insight in the main flame physics and the flame-flow interactions is given in Chapter 2. Chapter 3 goes on to explain the general idea behind the G-equation solver which is used in this thesis to model the flame motion. Subsequently the FTF theory is introduced and some of the aforementioned analytical velocity models for the FTF are presented and compared to each other. For the acoustic excitation, the velocity field has to be modeled. This is done in Chapter 4. In Chapter 5, the new model for u_{vol} is derived. Starting with potential sources in combination with conformal mapping, the potential sources are then modified to correct arising singularities from the potential sources. A first analysis of the impact of the gas expansion on the flame shape is analyzed in Chapter 6. Finally, the influence of the gas expansion on the FTF is investigated in Chapter 7.

2 Flame Physics and Flame Flow Interactions

Before deriving the new velocity model, it is first necessary to understand the relevant flame physics and in particular the flame flow interactions.

In Section 2.1, it is shown that a perfectly premixed flame front can be divided into two different zones, a preheating zone and a reaction zone. The reaction zone is dominated by diffusive processes, whereas in the preheating zone advection is also of importance. When the flame front is stretched, the diffusive processes can vary in direction and strength. This leads to an increase or decrease of the laminar burning velocity s_L, which denotes the propagation velocity relative to the fluid, see Section 2.2. Section 2.3 goes on to explain that the gas velocity increases when passing the flame front. This increase is caused by a negative density gradient as the temperature of the burnt gas is higher than of the unburnt gas. The decrease in density subsequently causes an increase in volume. The volume generated by a flame front is derived in Section 2.4. In Section 2.5 it is shown that due to pressure and density gradients barocline vorticity is generated. Both, barocline vorticity and volume production affects the upstream fluid and can lead to stream tube deflections, see Section 2.6. For a specific range of wave numbers, the flame front then becomes unstable. This instability is called the Darrius-Landau instability and is discussed in Section 2.7.

2.1 Flame Thickness and Flame Regions

Normally, the main chemical reaction between the fuel and the oxidizer takes place in the range of millimeters [16](Ch. 9). In the case of a standing flame front, unburnt premixed gas is streaming towards the flame front with a temperature T_u and leaves the flame front as burnt gas with the temperature T_b, see Figure 2.1. The heat that is emanated from the chemical reaction warms up the burnt gas, so that $T_b > T_u$. The difference between T_b and T_u is often in the range of thousands of Kelvin so that a huge temperature gradient arises. This gradient leads to a heat flux between the burnt and unburnt gas. Therefore, the unburnt gas is preheated till it reaches the burning temperature T_R and starts to react. In Figure 2.2, a temperature profile of a typical flame front is shown. It is also depicted that the flame front can be sub-divided into two different zones, the preheating zone where no chemical reaction appears and the reaction zone, where the main chemical reaction takes place [16](Ch. 9). The width of those two zones together is called the laminar flame thickness δ_f [16](Ch. 9).

Another important process is species diffusion, as the gas composition differs over the flame front. The reactants diffuse from the unburnt gas towards the flame front and burnt along with

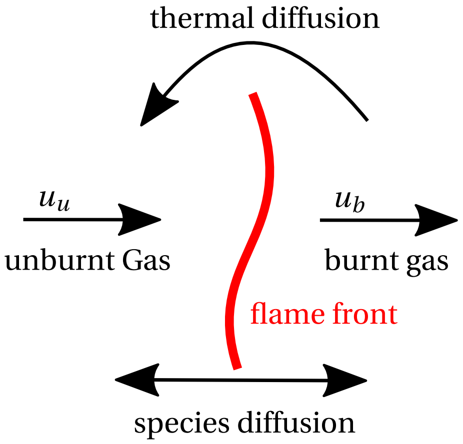

Figure 2.1: Unburnt gas streaming towards a standing flame front (—) and leaving it as burnt gas. Because of gradients in temperature and gas composition, thermal and species diffusion takes place.

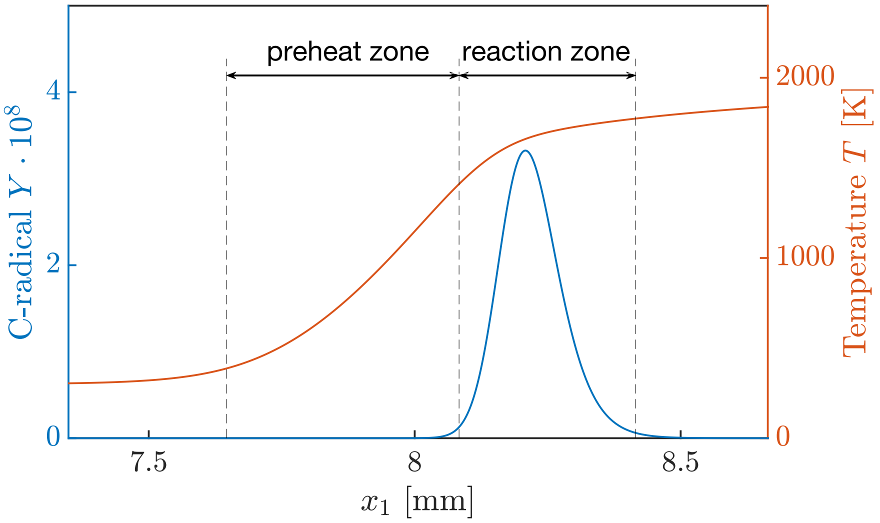

Figure 2.2: Temperature profile and the mole fraction of C-radicals profile in a methane-air flame within the vicinity of the flame front of which the center is located approximately at $x_1 = 8$ [mm]. Data was obtained by a simulation, generated by Steinbacher [23] with a GRI 3.0 mechanism.

reaction intermediates diffuse into the unburnt gas [16](Ch. 9), see Figure 2.1. Those reaction intermediates reduce the burning temperature T_R in the unburnt gas. Both temperature and species diffusion are important processes for the flame front. Which process dominates the flame physics, can be expressed with the Lewis number [16] (Ch. 9):

$$Le = \widehat{=} \frac{\text{temperature diffusion}}{\text{species diffusion}} \,. \tag{2.1}$$

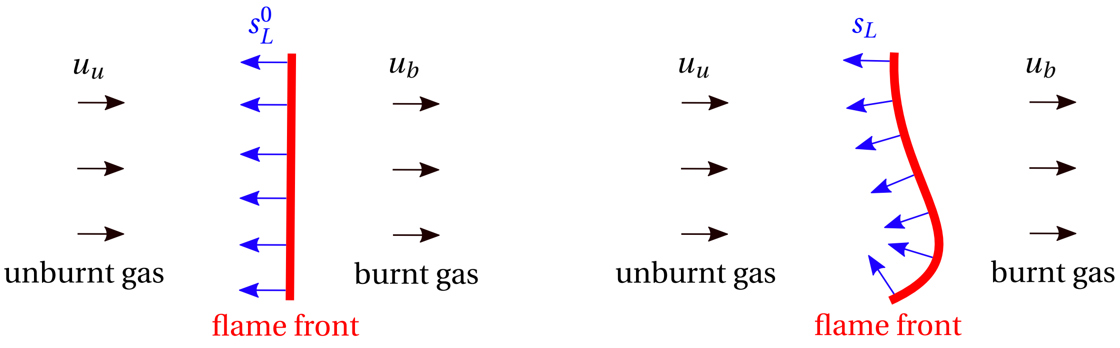

(a) (b)

Figure 2.3: Schematic representation of the laminar flame speed at the flame front (—). On the left side (a) is an unstretched flame front with the unstretched burning velocity s_L^0 depicted. On the right side (b), a curved flame front with the stretched burning velocity s_L is shown.

2.2 Laminar Flame Speed

As explained in Section 2.1, the flame front physics is dominated by diffusive processes, which preheat the unburnt gas to the burning temperature T_R, so that the chemical reaction takes place. Hence, the flame front is propagating relative to the gas. This relative propagating velocity is called the laminar burning velocity s_L and its direction is perpendicular to the flame front pointing towards the unburnt gas, see Figure 2.3. It is important to stress that the burning velocity can either be defined towards the unburnt gas ($s_{L,u}$), or towards the burnt gas ($s_{L,b}$).

s_L is not a constant and depends on the fuel mixture, the temperature and the pressure of the premixed gas as well as on the flame front geometry [16] (Ch. 9).

For instance hydrogen flames have a burning velocity $s_{L,u} \approx 2.5$ [m/s] [5], while methane flames normally burn with $s_{L,u} \approx 0.25$ [m/s] [16] (Ch. 9). The higher the unburnt gas temperature T_u is, the less energy is needed to reach the burning temperature T_R and therefore the unburnt gas reacts faster and s_L descends. Moreover, s_L declines with an increasing pressure, as $s_L \propto p^{-0.5}$ [16] (Ch. 9). It is denoted that the pressure differences p' along the flame front are small and therefore s_L is not locally affected by p'.

The most important thing in this thesis is the dependence of s_L towards the flame geometry. For an unstretched flame front with a constant gas velocity $\vec{u}$, the laminar burning velocity is often written as s_L^0, see Figure 2.3 (a). Flame stretching effects lead to an increase or decrease of the laminar burning velocity s_L. Those stretching effects alter the flame front geometry and can be expressed by the flame stretching rate κ as it was done by Lieuwen [16] (Ch. 9):

$$\kappa = \kappa_s + \kappa_{Curv} \, , \tag{2.2}$$

$$\text{with} \qquad \kappa_s = -\vec{n} \cdot \vec{n} : \nabla \cdot \vec{u} \qquad \kappa_{Curv} = -s_L \cdot (\nabla \cdot \vec{n}) \, .$$

The strain κ_s only exists if there are gradients in the velocity $\vec{u}$ along the flame front and is in particular responsible for flame stretching tangential to the flame front [16] (Ch. 9). κ_{Curv} represents the stretching effects from the curvature of the flame front [16] (Ch. 9). By multiplying the stretching rate κ with the Markstein length δ_M, one obtaines the formula for the influence of those stretching effects towards s_L [16] (Ch. 9):

$$s_L = s_L^0 - \delta_M \cdot \kappa \, . \tag{2.3}$$

The Markstein length scales with the thickness of the flame front and can be set in ratio with the laminar flame thickness δ_F, thus defining the Markstein number Ma [16] (Ch. 9):

$$Ma = \frac{\delta_M}{\delta_F} \, . \tag{2.4}$$

The Markstein length δ_M represents the sensitivity of the flame towards stretching effects [16] (Ch. 9), as examined in Section 2.7. It can be > 0 or < 0 depending on the gas mixture, and therefore the laminar burning velocity s_L can be bigger or smaller than the unstretched burning velocity s_L^0 [16] (Ch. 9). For most gas mixtures including the investigated case in this thesis, the laminar burning velocity $s_L > s_L^0$ for a concave (towards the unburnt gas) flame front as it is depicted in Figure 2.3 (b).

The reason why s_L changes due to stretching effects is that temperature and species diffusion vary with a curved flame front [16] (Ch. 9), and therefore the premixed gas burns faster or slower. Hence, the Markstein length is a function of the Lewis number *Le* [16] (Ch. 9), which has already been described in Section 2.1.

2.3 Velocity Acceleration through the Flame Front

As already described in Section 2.1, the incoming unburnt gas is heated while passing through the flame front. At the same time the density of the fluid decreases, see Figure 2.4. With the integral continuity equation:

$$\int_V \frac{\partial \rho}{\partial t} dV + \int_S \rho \cdot \vec{u} \cdot \vec{n} \, dS = 0 \, , \tag{2.5}$$

a relationship can be derived between the density ρ and the velocity u. Therefore a control volume with unit depth and unit height is set around the flame front, see Figure 2.5. Assuming a stationary unstretched flame front, which is the case for $\vec{u} = -\vec{s}_L^0$, the partial derivation after the time vanishes: $\frac{\partial}{\partial t} = 0$. Under the assumption that the fluid just flows perpendicular to the flame front, there is no fluid entering or leaving the control volume at the bottom or the top. Hence, Equation (2.5) then reduces to:

$$\rho_u \cdot u_u = \rho_b \cdot u_b \, . \tag{2.6}$$

The subscripts $(\cdot)_u$ and $(\cdot)_b$ represent the unburnt and the burnt fluid properties, respectively. With the expansion ratio E defined as

$$E = \frac{\rho_u}{\rho_b} \, , \tag{2.7}$$

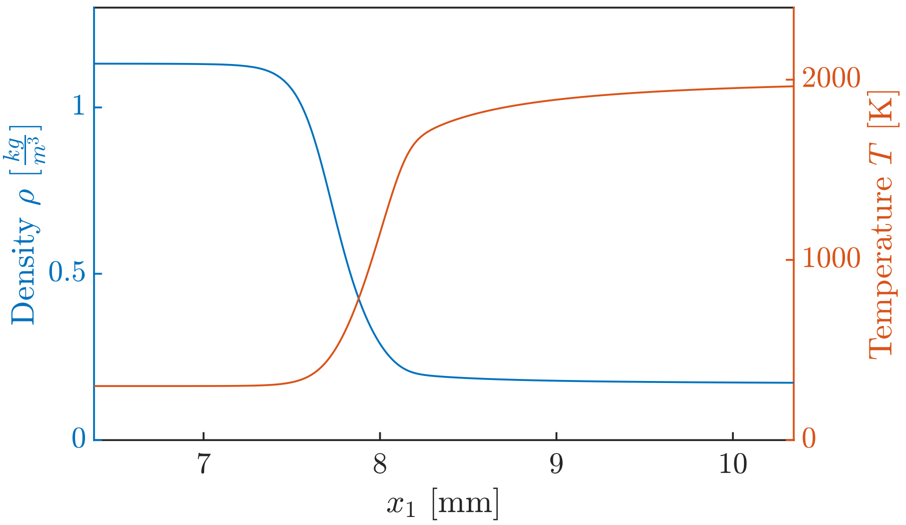

Figure 2.4: Temperature and density profile in a methane-air flame in the vicinity of the flame front, of which the center is located approximately at $x_1 = 8$ [mm]. Data was obtained by a Cantera simulation, produced by Steinbacher [23] with a GRI 3.0 mechanism.

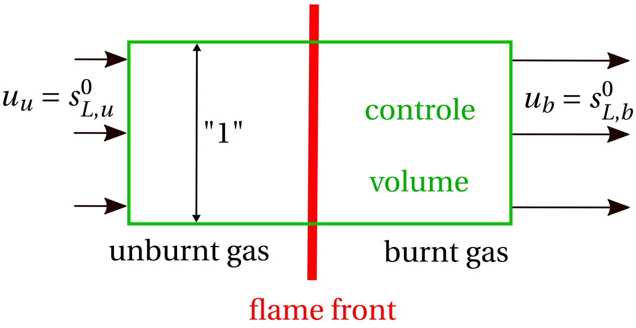

Figure 2.5: Control volume (🟩) with unit height and depth around an unstretched stationary flame front (🟥). Unburnt gas is entering the control volume with the velocity $u_u = s^0_{L,u}$ and leaving it as burned gas with the velocity $u_b = s^0_{L,b}$.

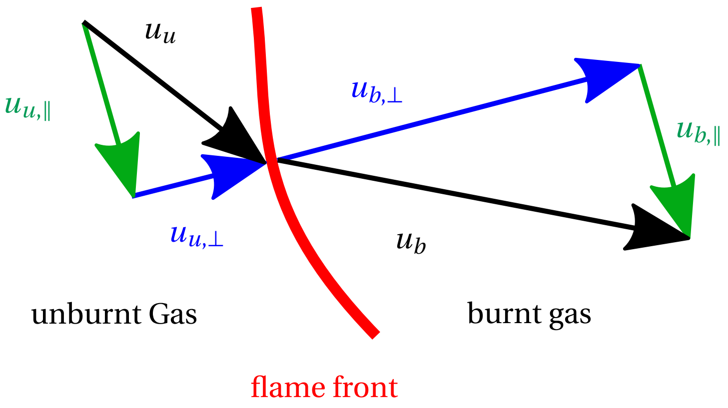

Figure 2.6: Schematic plot of the velocity of a fluid in the vicinity of a curved flame front (🟥). A fluid particle enters the flame front with the velocity u_u (⬛) and leaves it with the velocity u_b. Thereby, the tangential unburnt velocity component $u_{u,\|}$ (🟩) equals the tangential burnt velocity $u_{b,\|}$. The normal unburnt velocity component $u_{u,\perp}$ (🟦) is increased according to Equation (2.10).

the velocity difference before and after the flame front can be expressed as:

$$u_b - u_u = s^0_{L,u} \cdot (E - 1)\,. \tag{2.8}$$

As already mentioned, the derivation of Equation (2.8) is just valid under the assumption that $\vec{u} = -\vec{s}^0_L$. For a velocity $\vec{u} \neq -\vec{s}^0_L$, the flame front moves with the absolute flame velocity $\vec{v}_F = \vec{u} + \vec{s}^0_L$. To generalize the above derivation, the control volume can be moved with the flame front. Then the inlet velocity is s^0_L again and Equation (2.8) can be derived with the moving control volume.

In the case of a curved flame front, only the velocity normal to the flame front is accelerated according to Equation (2.8), the tangential velocity remains unaltered [16] (Ch. 9), see Figure 2.6. The relationship between the unburnt and burnt velocities then express as

$$u_{b,\|} - u_{u,\|} = 0 \tag{2.9}$$

$$u_{b,\perp} - u_{u,\perp} = s_{L,u} \cdot (E - 1)\,, \tag{2.10}$$

with the subscripts $(\cdot)_\perp$ and $(\cdot)_\|$ indicating the normal and tangential quantities to the flame front, respectively. Note that the unstretched burning velocity s^0_L from Equation (2.8) now becomes the stretched burning velocity s_L [16] (Ch. 9).

2.4 Flame Front is a Volume Source

As already mentioned in Section 2.3, a flame reduces the density of the incoming gas. Accompanied with that is an increase in fluid volume. This can be examined with the same approach which was already used in Section 2.3. The flame is assumed to be stationary, unstretched and a control volume is set, as depicted in Figure 2.5. The balance of volume entering and leaving the control volume is:

$$\dot{V}_E + \dot{V}_p = \dot{V}_l \,. \tag{2.11}$$

In the above equation $\dot{V}_E$, $\dot{V}_l$ and $\dot{V}_p$ represent the entering and leaving volume flux and the volume flux produced in that control volume, respectively. The entering and leaving volume flux in that control volume with unit height and unit depth are:

$$\frac{\dot{V}_E}{A} = u_u \tag{2.12}$$

$$\frac{\dot{V}_l}{A} = u_b \,. \tag{2.13}$$

Using the above equations and Equation (2.8), Equation (2.11) can be solved for the volume flux produced by the flame $\dot{V}_p$ per unit height and unit depth as:

$$\frac{\dot{V}_p}{A} = s^0_{L,u} \cdot (E-1) \,. \tag{2.14}$$

As $\dot{V}_p > 0$, a flame front acts as a volume source. Equation (2.14) can also be derived for an unburnt velocity $\vec{u} \neq -\vec{s}^{\,0}_L$ using the same technique with the moving control volume as in Section 2.3. It is denoted that the produced volume flux can vary when the flame front is curved. The reason for that is that the velocities $\vec{u}_u$ and $\vec{u}_b$ can vary along the flame front, see Section 2.7. To generalize Equation (2.14), $s^0_{L,u}$ has to be replaced by $s_{L,u}$ [19].

2.5 Barocline Vorticity Production at the Flame Front

Section 2.3 previously showed that the density and the velocity of a gas change while passing through a flame front. When analyzing the stationary integral momentum equation for a frictionless fluid without any external forces

$$\int_S \rho \cdot \vec{u} \cdot \vec{u} \cdot \vec{n} \, dS = -\int_S p \cdot \vec{n} \, dS \,, \tag{2.15}$$

one can derive that the static pressure also has to vary. Therefore a moving control volume is set, as in Section 2.3 and Section 2.4, around an unstretched flame front, see Figure 2.5. The velocities entering and leaving the control volume are $s^0_{L,u}$ and $s^0_{L,b} = s^0_{L,u} \cdot E$ (comp. derivation of Equation (2.8)) respectively. Then Equation (2.15) reduces to [16] (Ch. 7):

$$\rho_b \cdot (s^0_{L,b})^2 - \rho_u \cdot (s^0_{L,u})^2 = -p_b + p_u \,. \tag{2.16}$$

With the definition of the expansion ratio E, Equation (2.16) can then be solved for the pressure difference through the unstretched flame front:

$$p_b - p_u = (s^0_{L,u})^2 \cdot (1-E) \cdot \rho_u \,. \tag{2.17}$$

It is denoted that the relative pressure difference [16] (Ch. 7)

$$\frac{p_b - p_u}{p_u} = \mathcal{O}(M_u^2)\,, \tag{2.18}$$

is small as it is of the order of the square of the incoming Mach number M_u.

Equation (2.17) shows that in addition to the density gradient there is also a pressure gradient existing through the flame front. When those two gradients are not coaligned, barocline vorticity is produced. This vorticity production can be seen in the frictionless vorticity equation without any external body forces [16] (Ch. 7):

$$\frac{D\vec{\Omega}}{Dt} = (\vec{\Omega}\cdot\nabla)\cdot\vec{u} - \vec{\Omega}\cdot(\nabla\cdot\vec{u}) - \frac{\nabla\cdot p\times\nabla\cdot\rho}{\rho^2}\,. \tag{2.19}$$

Here, $\vec{\Omega}$ is the vorticity vector. The last term on the right side of Equation (2.19) represents the barocline vorticity production. It is obvious that no barocline vorticity is produced when the pressure and density gradients are coaligned. Equation (2.19) can be solved for a two dimensional stretched flame front as [16] (Ch. 7):

$$\Omega_b = \frac{\Omega_u}{E} - \left(1 - \frac{1}{E}\right)\cdot\left(\frac{u_u}{a_\Psi} + \frac{\partial u_u}{\partial s_\Psi}\right)\,. \tag{2.20}$$

Here, the vorticity points out of the two-dimensional plane. a_Ψ and s_Ψ are the radius of curvature of streamlines in the unburnt gas and the coordinate along a streamline respectively. Therefore, the vorticity in the burnt gas Ω_b is only dependent on the vorticity in the unburnt gas Ω_u and the curvature of the streamlines. When the flame front is unstretched, the last term in the brackets on the right hand side of Equation (2.20) vanishes and hence no barocline vorticity is produced [16] (Ch. 7).

2.6 Flame Front Influence on Upstream Flow

Because of volume production, the gas is accelerated normal through the flame front, see Section 2.3. In addition to that there is also an upstream influence of the flame front on the velocity field, see Figure 2.7 (a).

When a fluid element approaches a convex (towards the unburnt gas) part of the flame front, the pressure is increasing [16] (Ch.7). This pressure increase is illustrated in Figure 2.7 (b). For low Mach numbers in the unburnt gas, the relationship between the pressure and the velocity can be expressed with the stationary incompressible Bernoulli equation [16] (Ch.7):

$$p + \frac{\rho}{2}\cdot u^2 = const\,. \tag{2.21}$$

Hence, a pressure increase in flame direction leads to a velocity deceleration in flame direction, so that $\frac{\partial u_1}{\partial x_1} < 0$, see Figure 2.7 (b). The subscripts $(\cdot)_1$ and $(\cdot)_2$ denote the quantity in x_1 and x_2 direction. From the incompressible stationary continuity equation

$$\frac{\partial u_1}{\partial x_1} + \frac{\partial u_2}{\partial x_2} = 0\,, \tag{2.22}$$

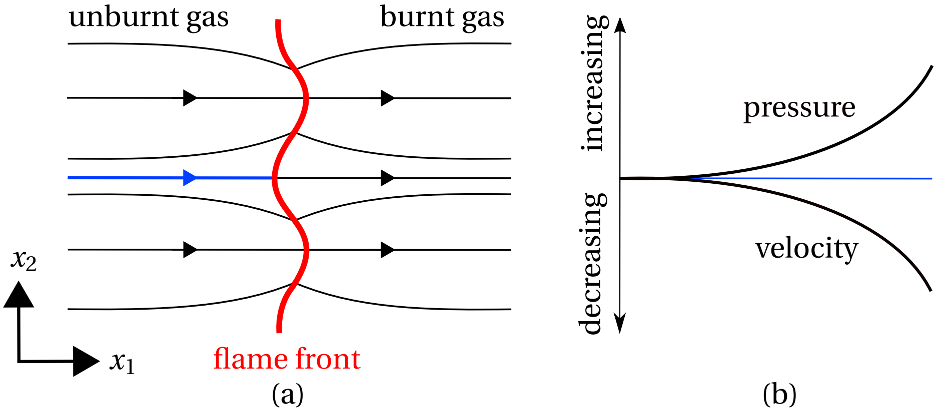

Figure 2.7: Streamline (▬) deflection at the flame front (▬) due to preheating effects and vorticity at the flame front (a). Pressure and velocity at the blue line (a) are qualitative shown on the right (b). Graphic design from (a) is inspired by Rhee [19], the qualitative pressure and velocity profile is adapted from Lieuwen [16] (Ch.7).

it can be seen that then $\frac{\partial u_2}{\partial x_2} > 0$. That means that a stream tube diverges and widens before the convex part of a flame front, see Figure 2.7 (a). In contrast to that, the stream tubes are forced to converge when approaching a concave part of a flame front.

It is questionable whether the volume production or barocline vorticity production dominates the stream tube deflection. A short discussion about the impact of the volume production is given in Section 7.3.

2.7 Darrius-Landau Instability

As described in Section 2.6, the gas is decelerated (accelerated) when approaching to a convex (concave) flame front. Consequently, the flame front is affected by a varying upstream velocity u_u. Under the assumption that the burning velocity s_L is constant, flame front deflections then increase as the absolute velocity $\vec{v}_F$ of the flame front varies, see Figure 2.8. Hence, every pertubation ξ with the wavenumber k grows in time and the flame front is unconditionally unstable [18]. This instability is called the Darrius-Landau instability.

The assumption that the burning velocity s_L is a constant, was already discussed in Section 2.3. In general, the burning velocity s_L decreases (increases) for a convex (concave) flame front and therefore the flame movement $\vec{v}_F$ is reduced. The growth rate σ_g of the perturbation ξ as a function of the perturbation wavenumber k is [18]:

$$\sigma_g = \frac{s_L^0 \cdot k}{1+E} \cdot \left(\sqrt{1 + k^2 \cdot \delta_M^2 - \frac{2 \cdot k \cdot \delta_M}{E} + \frac{1-E^2}{E}} - (1 + k \cdot \delta_M) \right) . \qquad (2.23)$$

For a growth rate $\sigma_g(k) < 0$, the flame front absolute stabilizes towards that specific perturbation wavenumber as the perturbation decreases in time [18]. Is $\sigma_g(k) > 0$, then the flame

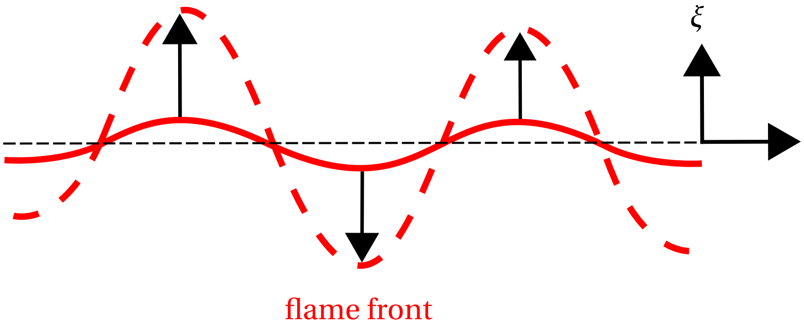

Figure 2.8: Schematic representation of an perturbed flame front (—). The perturbation ξ grows in time (- - -) due to the Darrius-Landau instability. Graphic design is inspired by Pitsch [18].

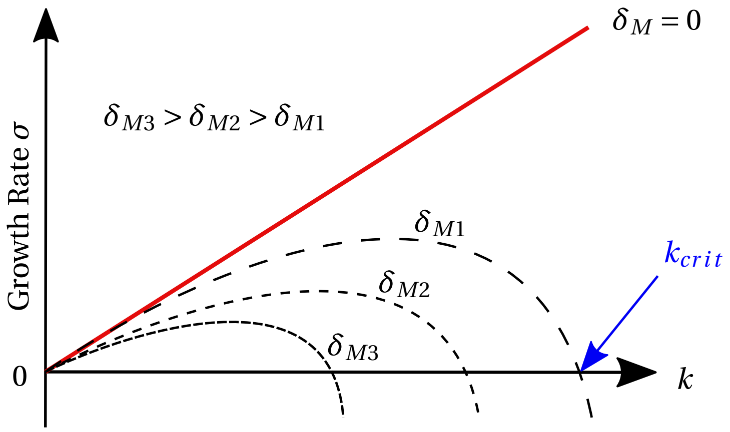

Figure 2.9: Schematic representation of the growth rate σ_g of an instability over the wavenumber k. With increasing δ_M, the value of the critical wave number k_{crit} decreases. The graph is adapted from [18].

front is unstable. The critical wavenumber k_{crit} up to which the flame front is unstable ($0 < k < k_{crit}$) depends on the Markstein length, see Figure 2.8. With increasing δ_M, the value of k_{crit} decreases [18]. Hence, thicker flame fronts are more stable than thinner flame fronts.

3 Flame Modeling and Flame Response

Chapter 2 gives a short insight into the flame physics and the flame flow interactions. Chapter 3 explains how theses effects can be modeled. Section 3.1 presents a mathematical description of the flame front movement, relying on the so called G-equation. It is explained that G is a scalar field which can be interpreted as a surface moving in space. For an accurate description of the flame front movement, the G-field needs to be a signed distance function. With usage of a simplified G-equation, it is possible to predict the response in heat release of a flame front towards an acoustic excitation. This response is called the flame transfer function (FTF), see Section 3.2 . It is explained that the FTF can be analyzed either in the time or in the frequency domain and each has it's advantages. For an analytic description of the FTF, several simplified velocity models are introduced. Those models are presented in Section 3.3 and briefly analyzed in both their accuracy and their physical motivation.

3.1 G-Equation

Some details of flame physics were already described in Section 2.1. This section outlines, how a flame front can be described in a mathematical manner. The flame front is treated as a discontinuous surface separating the unburnt gas from the burnt gas [12]. This surface is advected through the velocity $\vec{u}$ and moves relative to the gas with the burning velocity $\vec{s}_L$. In general, moving surfaces can be described with a Level-Set-Method as proposed by Sethian and Osher [17]. Therefore a n-dimensional surface is described in n+1 dimensions. Kerstein et al. [14] adopted one of Sethian's and Osher's Level-Set equations and expressed it as the so called G-equation:

$$\frac{\partial G}{\partial t} + \vec{u} \cdot \nabla \cdot G = s_L \cdot |\nabla \cdot G| \,. \tag{3.1}$$

In Equation (3.1), G is a scalar field depending on the location $\vec{x}$ and the time t. G is often chosen so that it states the shortest distance from a point $\vec{x}$ towards the flame front, which is thereupon located at $G = 0$ [20]. The sign of G is defined as $G < 0$ in the unburnt gas and $G > 0$ in the burnt gas [12], see Figure 3.1. Hence, the G-field is a signed distance function (SDF) and $|\nabla \cdot G| = 1$ with $\nabla \cdot G$ pointing towards the unburnt gas [20]. This SDF-property is important for the computational accuracy of the flame front movement, as it was already described by Satheesh et al. [20].

For a two-dimensional flame front, the G-field can be interpreted as a three-dimensional surface with the flame front as an isoline. This surface moves with the velocity $\vec{v}_F$, with reference to Section 2.2. It is denoted that s_L usually does not vary with the strain related stretch κ_s,

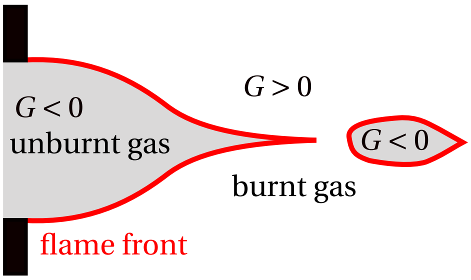

Figure 3.1: Schematic presentation of the G-field for a Bunsen flame front with a pocket formation. In the unburnt gas (grey), the sign of G is defined as $G < 0$ and in the burnt gas as $G > 0$.

as it was expressed in Equation (2.2) and Equation (2.3) and therefore only depends on the curvature κ_{curv} of the G-field.

As $\vec{u}$ can vary in the two-dimensional domain, the G-field can lose it's signed distance properties [20]. To counteract this, several methods exist. For instance the G-field can be reshaped to a signed distance field by solving the equation

$$\frac{\partial G}{\partial \tau} + sgn(G^0) \cdot \frac{\nabla \cdot G}{|\nabla \cdot G|} = sgn(G^0)\,, \tag{3.2}$$

as proposed by Sussman et al. [28]. In Equation (3.2), $sgn(G^0)$ is the sign function of the G-field and τ is a pseudo time step with which Equation (3.2) is iteratively solved until $|\nabla \cdot G| \approx 1$. Another method is to propagate the velocity $\vec{u}$ at the flame front normal to the flame front in the entire domain. This can be done with the so called Fast Marching Method, proposed by Adelsteinsson et al. [1]

3.2 Flame Transfer Function

When a flame front is acoustically excited, it responds to that excitation with a shifting in heat release $\dot{Q}$ [15]. This response can be expressed with the Flame Transfer Function (FTF), either in the time or the frequency domain [4]. To analyze the FTF, it is first necessary to divide the velocity and the heat release in its averaged $\bar{(\cdot)}$ and fluctuating $(\cdot)'$ quantities:

$$u = \bar{u} + u' \tag{3.3}$$

$$\dot{Q} = \bar{\dot{Q}} + \dot{Q}'\,. \tag{3.4}$$

In the frequency domain, the excitation signal u'_E and the fluctuating heat release $\dot{Q}'$ are connected by the frequency response (FR) function $F(\omega)$ as [25]:

$$\frac{\dot{Q}'}{\bar{\dot{Q}}} = F(\omega) \cdot \frac{u'_E}{\bar{u}_E}\,. \tag{3.5}$$

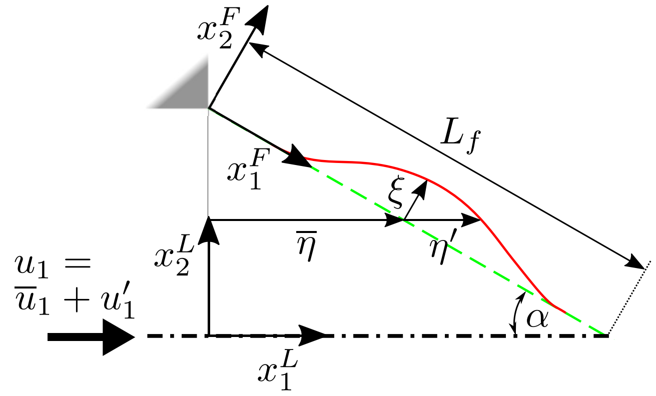

Figure 3.2: Illustration of two different coordinate systems. The flame aligned coordinate system x_F is aligned to the unperturbed flame front (- - -), with the flame front deflection ξ. The laboratory aligned coordinate system x_L describes the perturbed flame front position (—) with the unperturbed horizontal distance $\bar{\eta}$ and the disturbance distance η'. Also depicted is the flame length L_f and the angle towards the horizontal α. This figure is adopted from Steinbacher et al. [25].

$F(\omega)$ is often depicted in a bode diagram, with it's phase and magnitude plotted over the excitation frequency ω. The reason why the FTF is described in the frequency domain is that it is easy to analyze the behavior of the flame towards a certain excitation frequency.
As already mentioned, the FTF can also be analyzed in the time domain. Therefore, the flame is excited with a unit impulse $u_E' = \delta(t)$ [4]. The impulse response (IR) function $h(t)$ can be obtained with [25]:

$$\frac{\dot{Q}'}{\bar{\dot{Q}}} = h(t) * \frac{u_E'}{\bar{u}_E}\,. \tag{3.6}$$

In Equation (3.6) the mathematical operator " $*$ " expresses the temporal convolution $f * g \equiv \int f(\tau) \cdot g(x-\tau) d\tau$. The advantage of analyzing the FTF in the time domain is that it is often more easy to interpret the impact of some important flame attributes like time scales towards the FTF [4]. With system identification tools it is then possible to transform the IR in the FR and vice versa [25].
According to Lieuwen [15], the heat release fluctuation $\dot{Q}'$ can be calculated as:

$$\frac{\dot{Q}'}{\bar{\dot{Q}}} = \frac{\int_{x_F} \Delta h_R' dA}{\int_{x_F} \Delta \bar{h}_R d\bar{A}} + \frac{\int_{x_F} s_L' dA}{\int_{x_F} \bar{s}_L d\bar{A}} + \frac{A'}{\bar{A}}\,. \tag{3.7}$$

Equation (3.7) indicates that $\dot{Q}$ depends on s_L, the flame surface A and the heat of reaction Δh_R. For an analytical expression of the FTF, the change of heat release through s_L' and $\Delta h_R'$ is often neglected. Combining Equation (3.5) and Equation (3.6) with Equation (3.7) then results

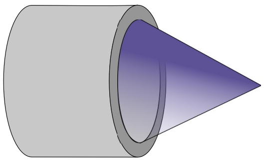

(a) Bunsen (conical Λ)

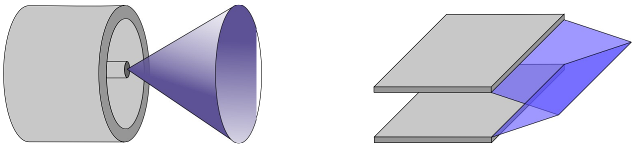

(b) Wedge (conical V)

(c) Slit

Figure 3.3: Schematic representation of different flames types. This diagram is adopted from Steinbacher et al. [25].

in:

$$\frac{A'}{\bar{A}} = F(\omega) \cdot \frac{u'_E}{\bar{u}_E} \tag{3.8}$$

$$\frac{A'}{\bar{A}} = h(t) * \cdot \frac{u'_E}{\bar{u}_E} \,. \tag{3.9}$$

An equation describing A was already presented in Section 3.1, the G-equation. Under the assumption that pertubations are small and that the velocity field is uniform, a first order analysis of the G-equation yields to

$$\frac{\partial \xi}{\partial t} + \bar{u}_{\parallel} \cdot \frac{\partial \xi}{\partial x_{1,F}} = u'_{\perp} \,, \tag{3.10}$$

see, e. g., Schuller er al. [22]. In Equation (3.10), ξ is the perturbed flame position in a flame aligned coordinate system x^F, see Figure 3.2. It is also possible to transform Equation (3.10) in a laboratory fixed coordinate system x^L, see e.g. Steinbacher et al. [25]:

$$\frac{\partial \eta'}{\partial t} - \cos(\alpha) \cdot \sin(\alpha) \cdot \bar{u}_1 \cdot \frac{\partial \eta'}{\partial x_2^L} = u'_1 + \frac{\cos(\alpha)}{\sin(\alpha)} \cdot u'_2 \,. \tag{3.11}$$

Here η' is the horizontal flame front deflection and α is the flame angle towards the horizontal line , see Figure 3.2. Both Equation (3.10) and Equation (3.11) express the flame front position dependent on the velocity u and can be integrated to obtain the flame surface area A. As discussed by Steinbacher et al. [25], it is important to consider which coordinate system is chosen for the integration, as a special treatment of the boundaries may be necessary depending on the flame type. An overview of the most common flame types is depicted in Figure 3.3.

3.3 Velocity Models for the FTF Prediction

For an analytical expression of the flame transfer function, it is necessary to derive a simplified expression of the distorted velocity u' at the flame front, see Equation (3.10).

In Section 2.6 it was previously shown that the flame front affects the velocity field due to barocline vorticity production and heat release. Both processes are very complex and so their influence along the flame front on u' is hard to describe analytically. Furthermore, u' is affected by the excitation u'_E, depending on the combustor geometry, see Chapter 4.

There still exists several simplified models which are presented in this section. In general, one can distinguish those models in acoustic based models (Section 3.3.1) and convective models (Section 3.3.2).

Their impact on the IR is explained and the corresponding FR is shown. Subsequently, the IR and FR of those models are compared to numerical results, obtained by CFD simulations. Those simulations were made by Steinbacher et al. [26] for a backward facing step duct geometry, with a feed channel radius of $R_i = 5\ [mm]$ and a confinement ratio of $C_r = R_i/R_a = 0.66$ and $C_r = 0.4$, see Figure 4.2. R_a denotes the combustor radius. The physical interpretation technique used in this section is adopted from Blumenthal et al. [4]. They described the responsible processes for the linear flame response of Bunsen and Wedge Flames. It is denoted that this section is restricted to Slit flames, as the differences between the velocity models are most pronounced. Despite this, the techniques from Blumenthal et al. [4] can be used without alterations. Details about the influence of velocity models on the FTF of other flame types can be seen in [25] or [4].

3.3.1 Acoustic Based Velocity Models

Acoustic velocity models are based on neglecting the influence of the flame on u' and only modeling the acoustic response to the excitation u'_E. In Section 4.1 it will be shown that the domain is acoustic compact [26] and a simplified relation between u' and u'_E yields to the Laplace equation. An important property of the Laplace equation is that the solution adjusts immediately, as the equation does not contain any time derivation $\frac{\partial}{\partial t}$. Hence, the boundary condition u'_E affects u' at the entire flame front without any time lag.

Consequently, Fleifil et al. [12] proposed the uniform velocity model. This model was derived in a duct geometry without area jumps and is a solution of the Laplace-equation. The velocity fluctuation u' for the IR then expresses as [4]:

$$u'_1 = u'_E = \delta(t) \qquad u'_2 = 0\,. \tag{3.12}$$

In the above equation $\delta(t)$ denotes the Delta function. Due to that impulse excitation, the flame front is immediately advected downstream in the x_1^L direction, see Figure 3.4 (a). When the flame front is stabilized at the burner rim, it then restores itself with the restoration velocity u_r in the x_1^F direction. The restored part of the flame front consumes the incoming unburnt gas, so that the perturbed part of the flame front is stifling, see Figure 3.4 (b). The overlap Δ_o arises and increases the flame front surface area. Δ_o is transported downstream with u_r until

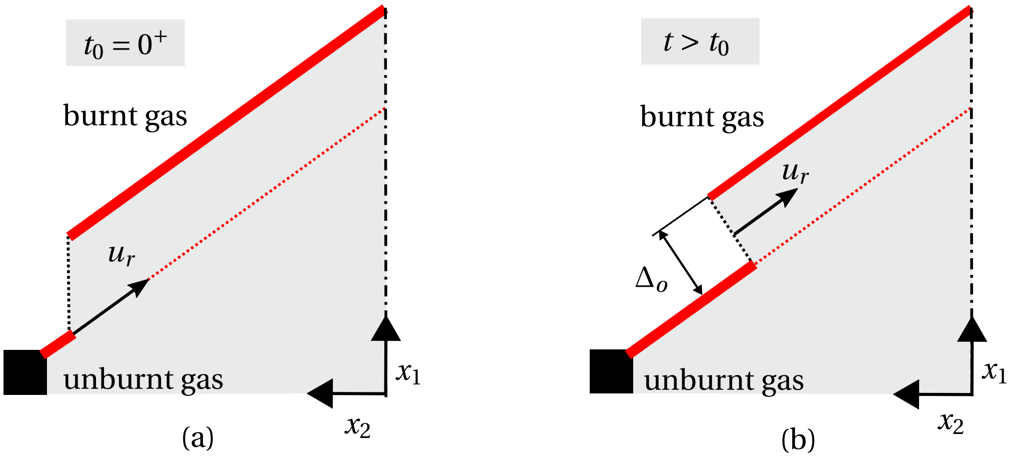

(a) (b)

Figure 3.4: Depicted is a displaced flame front (—), anchored at the burner rim. The initial flame front restores itself with the velocity u_r (a). For later times (b) an overlap Δ_o arises which travels with the velocity u_r along the flame front. The unburnt gas is depicted in grey. Diagram is adapted from Blumenthal et al. [4].

it reaches the flame tip and vanishes. The time it takes for the overlap to advect from the flame base to the flame tip is called τ_r and is a typical timescale for the flame restoration process. τ_r can be expressed as [26]:

$$\tau_r = \frac{R_i}{s_L \cdot \cos(\alpha)} \,. \tag{3.13}$$

The normalized IR function $h^* = h \cdot \tau_R$ plotted over the normalized time $t* = t/\tau_r$ can be seen in Figure 3.5. Also depicted is the FR magnitude and the FR frequency plotted over the Strouhal number $f^* = \omega/(2 \cdot \pi \cdot \tau_r)$. The IR of the uniform model (- - -) directly jumps to $h^* = 1$ at the time $t = 0^+$, when Δ_o is created, as $A' > 0$. At $t^* = 1$ $(t = \tau_r)$, when the overlap reaches the flame tip and vanishes, the IR decreases to the value $h^* = 0$, as the flame front is restored and subsequently $A' = 0$. Comparing the FTF prediction to the FTF obtained by the CFD simulation (—), it can be seen that the FR magnitude is underestimated by the uniform model. In addition to that, the phase does not correspond to the numerical results.

The reason for that is that the uniform velocity model was developed for Bunsen flames in a duct without any area jump. The area jump leads to a higher velocity fluctuation u' at the flame base than at the flame tip, see Figure 4.5. Furthermore, Slit flames are very sensitive towards any kind of flame tip movement [25] and so the velocity difference in u' along the flame front is of importance.

An improvement of this was made with the Flame-Foot-Displacement (FFD) model, proposed by Steinbacher et al. [26]. The FFD model uses a triangular velocity profile, where $u'_\perp = 2 \cdot \sin(\alpha) \cdot u'_E / f_b$ at the flame base and shrinks towards the flame tip. This velocity profile is a better approximation for u', but does not satisfy the local continuity equation [26]. The parameter f_b can be used to fit the initial flame foot displacement [25].

The IR predictions of the FFD model (- - -) can capture the first deflection of the impulse response as well as improving the phase predictions towards the uniform model. It is, how-

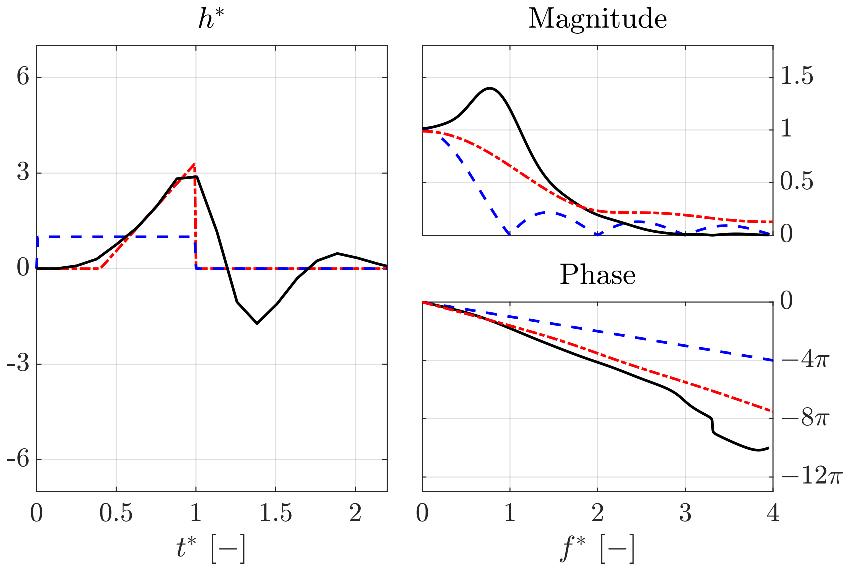

Figure 3.5: Predictions for the FTF of Slit flames from the Uniform model (---)($\tau_r = 18.7$ [ms]) and the FFD model (-·-) ($\tau_r = 18.7$ [ms]), compared with results from a CFD simulation (—) ($\tau_r = 11.4$ [ms]). The simulation was made by Steinbacher et al. [26] for a backward facing step duct geometry, with a feed channel height of $R_i = 5$ [mm] and a confinement ratio of $C_r = 0.66$.

ever not able to predict the high deflection of the FR magnitude about $f'* = 0.8$. The second and third deflection of the impulse response are also not captured. This is due to the missing flame-flow feedback towards u' [26]. The predictions of the FTF of Slit flames worsen for smaller confinement ratios C_r. Further discussion about this effect can be seen in Section 7.3. It is noted that for the above comparison the timescale τ_r was smaller for the CFD simulation than for the theoretical models. This is due to the fact that the bulk flow speed is increased in the CFD simulation.

3.3.2 Convective Velocity Models

Experiments of the flame behavior towards acoustic excitation, lead to the observation that the excitation signal is convected with the bulk flow as waves in an axial direction [2], see Figure 3.6. Those waves arise due to the flame-flow feedback [2]. According to Birbaud et al. [2], the motion of the unburnt gas is dominated by those waves, especially in the range of low Strouhal numbers. With an increasing Strouhal number, the acoustics get more important.
Based on that convective behaviour, Schuller et al. [22] proposed the so called convective velocity model. The excitation signal u_E' is transported with the bulk flow in the axial direction x_1^L and has no velocity in the x_2^L direction. The velocity can then be written for the IR as:

$$u_1' = \delta\left(t - \frac{x_1^L}{\bar{u}}\right) \qquad u_2' = 0\,. \tag{3.14}$$

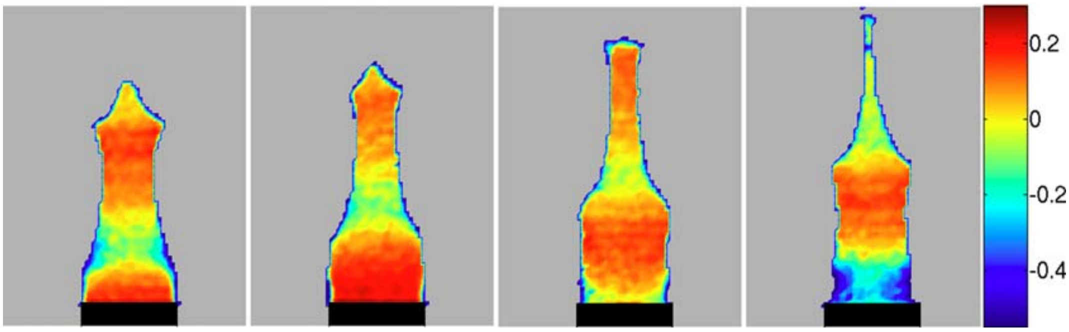

Figure 3.6: Experimental velocity observation of a conical flame front. Plotted is the velocity fluctuation in the axial direction u'_1 in [m/s], for an excitation frequency $f_0 = 70$[Hz] at four instants $\phi = 0, \pi/4, \pi/2, 3\pi/4$. The figure is adopted from Birbaud et al. [2].

In terms of flame aligned coordinate system, the impulse is convected with the velocity u_c along the flame front, see Figure 3.7. By virtue of that impulse, the flame is excited at the position of the impulse and the gap Δ_g arises. The flame front then restores itself, as explained for the uniform model. The gap and the overlap neutralize each other and as long as both exist the flame front surface is not affected. The time it takes for the gap to reach the flame tip is τ_c [26]:

$$\tau_c = \cos(\alpha) \cdot \tau_r \, . \tag{3.15}$$

As $\tau_c < \tau_r$, first the gap and then the overlap reach the flame tip and vanish. Hence, the flame front surface is first increased so that $A' > 0$ and then decreased so that $A' = 0$ again.
This increase at $t^* = \tau_c/\tau_r$ $(t = \tau_c)$ and decrease $t^* = 1$ $(t = \tau_r)$ can also be seen in the IR of the convective model (- - -), see Figure 3.8. Comparing the FR prediction with results from a CFD simulation (—) with a confinement ratio of $C_r = 0.4$, it can be seen that the phase aligns reasonable well, but the magnitude is underestimated for small f^* and does only slowly decrease to zero for higher f^*. In addition to that, the convective model does not satisfy the local continuity equation.

Therefore, Cuquel et al. [11] proposed the convective incompressible velocity model. This model is based on the convective model from Schuller et al. [22], as it adopts the velocity in the axial direction u'_1. The velocity in x_2^L direction is determined so that it fulfills the local continuity equation:

$$u'_2 = -x_2^L \cdot \frac{\partial u'_2}{\partial x_1^L} \, . \tag{3.16}$$

The velocity component in x_2^L increases the local displacement from the impulse compared to the convective model. This reflects in the IR of the convective incompressible model (- - -) in a higher h^*. In addition to that, a negative impulse (•) arises at $t^* = 1$.
The FR prediction can now capture the magnitude of the CFD results up to a Strouhal number of $f^* = 1.5$. For $f^* > 1.5$ the magnitude is highly overestimated. The typical cut off frequency of the FR is no longer to be able to forecast, due to the impulse at $t^* = 1$. The phase prediction

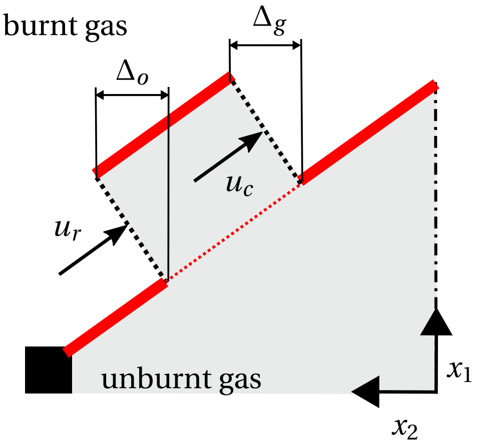

Figure 3.7: Depicted is a displaced flame front (—), anchored at the burner rim. The overlap Δ_o and the gab Δ_g travel along the flame front with the velocities u_r and u_c, respectively. The unburnt gas is depicted in grey. Diagram is adapted from Birbaud et al. [2].

improved compared to the convective model.

To obtain the typical cut off frequency, Steinbacher et al. [25] mixed the convective incompressible model with a Gaussian kernel (CIG-model) instead of the Dirac-delta function (CID-model). The velocities then expresses as:

$$u_1' = g\left(t - \frac{x_{1,}^L}{K \cdot \bar{u}_1}\right) \tag{3.17}$$

$$u_2' = \frac{x_2^L}{K \cdot \bar{u}_1} \cdot g'\left(t - \frac{x_1^L}{K \cdot \bar{u}_1}\right), \tag{3.18}$$

with the definition of the Gaussian kernel:

$$g(\tau) = \frac{1}{\sqrt{2 \cdot \pi \cdot \sigma^2}} \cdot exp\left(-\frac{\tau^2}{2 \cdot \sigma^2}\right). \tag{3.19}$$

Here g' is the derivative of the Gaussian kernel and σ denotes the standard deviation. K is a parameter that increases the convection speed of the Gaussian kernel, which can be used to fit the IR. The advantage of the Gaussian Kernel is that it disperses the impulse at $t^* = 1$ from the CID model in time, and therefore the high magnitude for higher frequencies is damped. Both the IR and FR predictions of the CIG model improved compared to the CID-model, see Figure 3.8. The IR can now capture the oscillating IR and also the magnitude of the FR is a good approximation of the CFD result. It is noted that the CIG model seems to alter the characteristic timescale τ_r. This is the reason why the oscillating IR is higher and starts at an earlier t^*. When τ_r is adjusted so that the CIG-model and the CFD result start oscillating at the same time, both FTFs are well aligned [25].

Especially for bunsen flames, the convective models have a better prediction of the FTF than

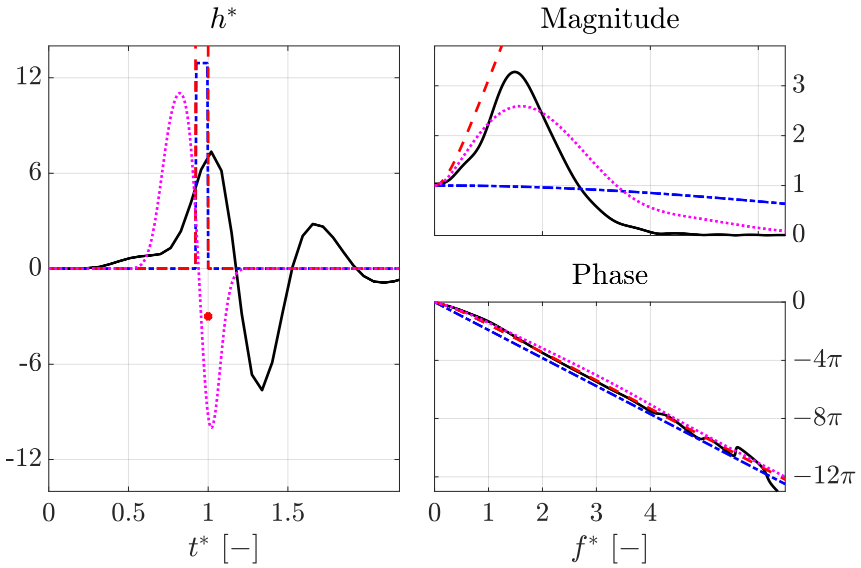

Figure 3.8: Depicted are FTF of Slit flames from the convective model (- - -) (τ_r = 18.7 [ms]), the CID model (- · -) (τ_r = 18.7 [ms]) and the CIG model (· · · ·) (τ_r = 18.7 [ms]), compared with results from a CFD simulation (—) (τ_r = 15.7 [ms]). The simulation was made by Steinbacher et al. [26] for a backward facing step duct geometry, with a feed channel height of $R_i = 5$ [mm] and a confinement ratio of $C_r = 0.4$.

the acoustic based models, but the question of the dominating effect leading to the convective waves arises.

4 Acoustic Modeling

Before the impact of the gas expansion on the FTF can be analyzed, it is necessary to model the acoustics. Therefore in Section 4.1 the governing equation for the acoustic velocity field is derived. With the assumptions of an inviscid flow without flame-flow feedback, the acoustics obey the Laplace-equation. A technique called mapping is introduced in Section 4.2, which simplifies the boundary condition treatment of the Laplace-equation for an analytical solution. A simple duct geometry is given as an example to explain the mapping technique (Section 4.2.1). Furthermore, a more complex mapping is applied to solve the acoustic velocity field in a duct geometry with a backward facing step (Section 4.2.2). As the resulting velocity field exhibits a singularity at the flame base, a Kutta-condition, derived by Steinbacher [23], is applied in the form of a vorticity panel (Section 4.2.3).
It is noted that even though the acoustic velocity field u'_{ac} is modeled, the derived equations are valid for every potential velocity field u_{pot}. Hence, in the following the term u_{pot} is used instead of u'_{ac}.

4.1 Governing Equation

According to Chu and Kovasznay [9], every distortion can be separated into three different modes: the vorticity mode, the sound mode and the entropy mode. In the absence of walls, those three modes do not interact in terms of linearized theory [9]. As the excitation signal for the flame front is small and of acoustic type, the vorticity and the entropy mode can be neglected. That means that an acoustic excitation only leads to an acoustic velocity perturbation. As shown by Steinbacher et al. [26], for the acoustic velocity field, only the potential part needs to be considered. The acoustic velocity field then obeys a potential Φ and can be calculated with the gradient of this potential as:

$$\nabla \cdot \Phi = \vec{u}_{pot} \,. \tag{4.1}$$

For the potential Φ, a non-dimensional wave equation can be derived, see e.g. [26].

$$\mathrm{He}^2 \cdot \frac{\partial^2 \Phi^*}{\partial t^{*2}} - \frac{\partial^2 \Phi^*}{\partial x_i^* \partial x_j^*} = 0 \,, \tag{4.2}$$

In Equation (4.2), He denotes the Helmholtz number. As it was described by Steinbacher et al. [26], the Helmholtz number can be expressed with the Mach number M and the Strouhal number f^* as $\mathrm{He} = \mathrm{M} \cdot f^*$. For the Strouhal number, only values up to $f^* = 10$ [26] need to be considered, as the flame responds to higher frequencies with a diminishing FR magnitude, see Figure 3.8. As bulk flow values are small, the Helmholtz number is of the order $\mathcal{O}(10^{-1})$ and the first term on the left side of Equation (4.2) can be neglected [26]. The resulting governing equation for the acoustic velocity field then reduces to the Laplace equation [26]:

$$\nabla^2 \Phi = 0 \,. \tag{4.3}$$

It is denoted that for the derivation of Equation (4.2), it was assumed that there is no interaction between the flame and the acoustics. In general, the heat release of the flame front leads to a gas expansion subsequently producing pressure waves, which affect the acoustic mode [9].

The impact of neglecting the influence of the flame front towards the acoustic velocity field is shortly discussed in Section 4.2.3.

4.2 Solving the Laplace Equation with Conformal Mapping

To solve the Laplace equation, two conformal mappings from Brown and Churchill [7] (Appendix 2) are applied for two different duct geometries in which the flame front is located.
An important property of the conformal mapping is that potential lines and streamlines are perpendicular in both the physical and in the mapped domain (also referred to as the image domain). This means that a potential velocity field stays a potential velocity field, even when it is mapped. Only the potential function changes due to the different coordinates.
The advantage of using the mapping to solve the Laplace-equation is that the boundary condition treatment is often simplified in the image domain. It is then easier to find a solution for the potential Φ in the image domain and can afterwards evaluate the velocity in the physical domain.
In the following, the complex physical domain is described with the coordinates $x = x_1 + i \cdot x_2$ and the mapped complex image domain with $\xi = \xi_1 + i \cdot \xi_2$, see Figure 4.1. The velocity in the physical domain is defined as $u = u_1 + i \cdot u_2$.

4.2.1 Exponential Function Mapping

Before a conformal mapping can be applied, it is first necessary to define the boundary conditions for the Laplace-equation. In this section, the potential velocity field is searched for in a simple duct geometry with walls (—) located at $x_2 = 0$ and $x_2 = i \cdot D$, with D denoting the duct diameter, see Figure 4.1.These walls should be non-slip walls and impermeable, hence they possess the same properties as a streamline. At the inlet of the duct geometry at $x_1 = -\infty$ the velocity u_E is imposed. As the Laplace equation describes an inviscid and incompressible flow, the same velocity should be able to leave the duct geometry at $x_1 = \infty$. The expected solution u_{pot} for the potential velocity field is a flow from $x_1 = -\infty$ towards $x_1 = \infty$, see the streamlines (—) in Figure 4.1 (a).
To simplify the boundary condition treatment, an exponential function mapping is used:

$$\xi = exp\left(\frac{x \cdot \pi}{D}\right) \,. \tag{4.4}$$

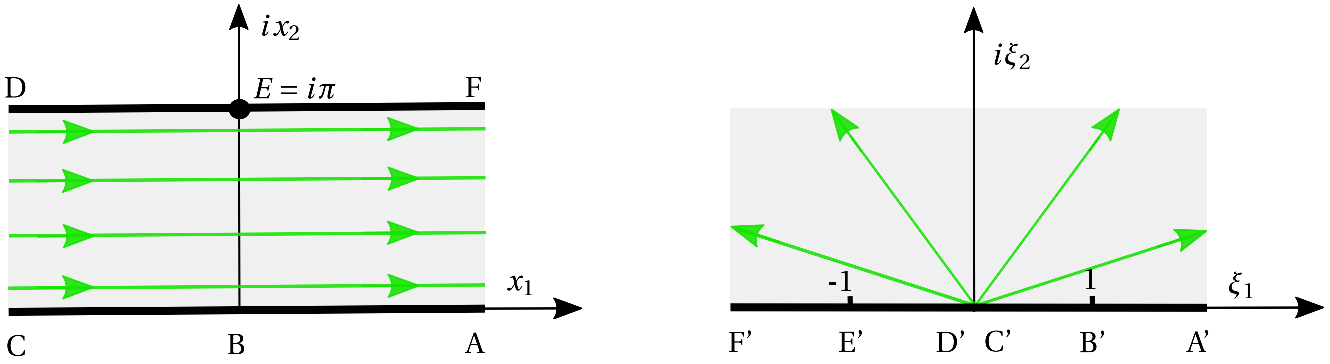

(a) physical domain

(b) image domain

Figure 4.1: Visualization of the exponential function mapping. The points A-E in the complex physical domain (a) are mapped to the points A'-E' in the complex image domain (b). The duct walls (—) located at $x_2 = 0$ and $x_2 = i \cdot \pi$ are mapped to the ξ_1 axes in the image domain. The area in between the duct walls (grey space), is mapped to the upper half ($\xi_2 > 0$) of the image domain. Also depicted are streamlines (—) of the potential velocity field in both domains.

By evaluating the above equation, one can see that the walls are mapped to the real ξ axes in the image domain, see Figure 4.1. The corresponding boundary condition for the potential Φ_ξ in the image domain then reduces that the ξ_1 axes should become a streamline. The area in between the duct geometry in the physical domain (grey space) is mapped to the upper half of the complex image domain ($\xi_2 > 0$), see Figure 4.1. Everything outside of the duct geometry is mapped to the lower half of the complex image domain ($\xi_2 < 0$). The inlet and outlet of the duct geometry in the physical domain are mapped to the origin and to infinity, respectively. Therefore a stream radiating from the origin towards infinity is expected in the image domain, see the streamlines (—) in Figure 4.1(b). The solution for the potential Φ_ξ is a source located at the origin $\xi = 0$. The corresponding potential is:

$$\Phi_\xi = \frac{\dot{V}_{p,s}}{2 \cdot \pi} \cdot \ln \xi \,. \tag{4.5}$$

Here, $\dot{V}_{p,s}$ denotes the volume flux that is produced by the source. In general, the streaming volume flux should be the same in both domains. The volume flux entering the duct geometry in the physical domain is $\dot{V}_E = u_E \cdot D$, this would lead to an equal volume flux streaming towards the upper half of the complex ξ domain ($\xi_2 > 0$). As the source can radiate it's volume in both the upper and the lower half of the image domain, it's strength $\dot{V}_{p,s}$ should be double the strength of the entering volume flux $\dot{V}_E$ in the physical domain:

$$\dot{V}_{p,s} = 2 \cdot u_E \cdot D \,. \tag{4.6}$$

Once the potential in the image domain is found, the velocity can directly be evaluated in the physical domain simply by using the chain rule [7] (Ch. 11) :

$$\tilde{u}_{pot}(\xi) = \frac{\partial \Phi_\xi}{\partial \xi} \cdot \frac{\partial \xi}{\partial x} = \frac{\partial \Phi_\xi}{\partial \xi} \cdot \left(\frac{\partial x}{\partial \xi} \right)^{-1} \; . \tag{4.7}$$

Here, the superscript $\tilde{(\cdot)}$ denotes the complex conjugated quantity. With the above equation, one can simply map a point x from the physical domain to the image domain ξ and subsequently evaluate it's velocity in the physical domain. For the chosen mapping with the potential Φ_ξ from Equation (4.5), the velocity field is:

$$u_{pot} = \tilde{u}_{pot} = \frac{V_{p,s}}{2 \cdot D} \; . \tag{4.8}$$

With the source strength of Equation (4.6), the velocity field then reduces to:

$$u_{pot} = u_E \; . \tag{4.9}$$

The above solution for the velocity field in the duct geometry could also be estimated without the mapping. Despite this, the technique in this section can be applied for other more complex duct geometries.

4.2.2 Schwarz-Christoffel Mapping

For evaluating the FTF, in general a duct geometry with a backward-facing step is applied, see Figure 4.2(a). Therefore the Laplace-equation needs to be solved once again, as it was already done is Section 4.2.1.

Before solving the Laplace-equation, it is first necessary to define the boundary conditions. As the geometry is symmetric, only half of the duct geometry needs to be solved. The symmetry line (- - -), as well as the walls (—), should therefore become a streamline. The inlet velocity at $x_1 = -\infty$ is u_E. The volume flux $\dot{V}_E = R_i \cdot u_E$, passing through half of the duct, should be able to leave the duct at $x_1 = \infty$.

For the mapping, a Schwarz-Christoffel (SC) transformation is applied, as it was already done by Steinbacher et al. [26]. The SC transformation is a technique which maps a real axes in a complex domain to an arbitrary polygon [7] (Ch. 11). Here, the real axes is the ξ_1 axes in the image domain and the polygon is half of a duct geometry (including symmetry line) with a backward-facing step in the physical domain x, see Figure 4.2. Hence, the Schwarz-Christoffel transformation gives only an analytical expression for the mapping from the image domain to the physical domain [26]:

$$x(\xi) = \frac{R_a}{\pi} \cdot \left[\cosh^{-1}\left(\frac{2 \cdot C_r^2 \cdot \xi - 1 - C_r^2}{1 - C_r^2} \right) - C_r \cdot \cosh^{-1}\left(\frac{(1 + C_r^2) \cdot \xi - 2}{(1 - C_r^2) \cdot \xi} \right) \right] \; . \tag{4.10}$$

Here C_r denotes the confinement ratio $C_r = R_i / R_a$. If one wants to map from the physical to the image domain, the above equation needs to be solved numerically.

The boundary conditions reduce in the image domain to the same of Section 4.2.1. The ξ_1

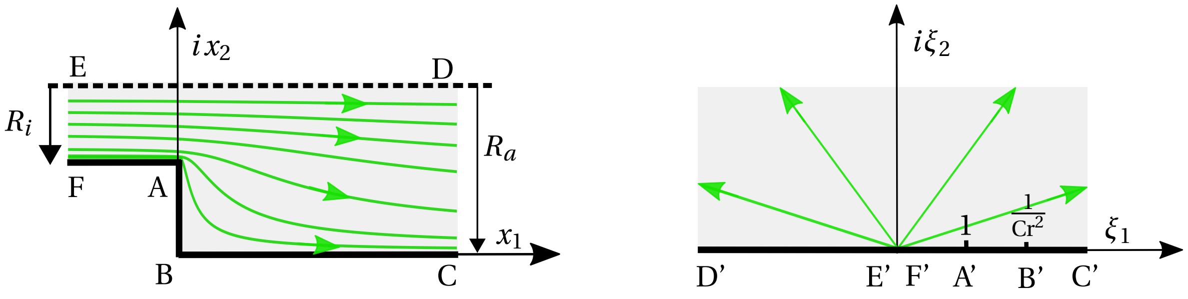

(a) physical domain

(b) image domain

Figure 4.2: Visualization of the Schwarz-Christoffel mapping. The points A-E in the complex physical domain (a) are mapped to the points A'-E' in the complex image domain (b). The duct walls (—) and the centerline (- - -) of the duct geometry are mapped to the ξ_1 axes in the image domain. The area in between the duct walls and the centerline (grey space) is mapped to the upper half ($\xi_2 > 0$) of the image domain. Also depicted are streamlines (—) of the potential velocity field in both domains.

axes should become a streamline. The solution of the Laplace-equation is once again a source in the origin. The velocity can then be evaluated with Equation (4.7). Therefore the inverse derivation $\left(\frac{\partial x}{\partial \xi}\right)^{-1}$ from Equation (4.10) is needed [26]:

$$\left(\frac{\partial x}{\partial \xi}\right)^{-1} = \frac{\pi}{R_a}\cdot\frac{\sqrt{\xi-\frac{1}{C_r^2}}}{\sqrt{\xi-1}}\cdot\xi\,. \tag{4.11}$$

By multiplying the above equation with the derivation $\frac{\partial\cdot}{\partial\xi}$ of the source potential from Equation (4.5), one obtains the conjugate complex velocity $\tilde{u}_{pot}$ in the physical domain dependent of it's mapped location ξ:

$$\tilde{u}_{pot}(\xi) = \frac{R_i}{R_a}\cdot\frac{\sqrt{\xi-\frac{1}{C_r^2}}}{\sqrt{\xi-1}}\cdot u_E\,. \tag{4.12}$$

For the above equation, it was once again used that the strength $\dot{V}_{p,s}$ of the source is double the entering volume flux $\dot{V}_E$. The corresponding streamlines (—) in the physical domain as well as in the image domain can be seen in Figure 4.2.

4.2.3 Kutta-Condition

In a real fluid flow, the fluid is not able to follow the abrupt direction change at the corner A (Figure 4.2) in the backward facing step duct geometry as predicted by the Laplace-equation solution. Normally, the fluid streams parallel to the feed channel in the combustion chamber and vorticity is shed at the corner. This unrealistic behavior can also be seen in the solution of the potential velocity field from Equation (4.12), as the velocity becomes infinitely high at the corner A. To correct this, a Kutta-condition was derived by Steinbacher [23]. The Kutta-condition corrects the potential Φ_ξ in the image domain so that the fluid leaves the feed duct

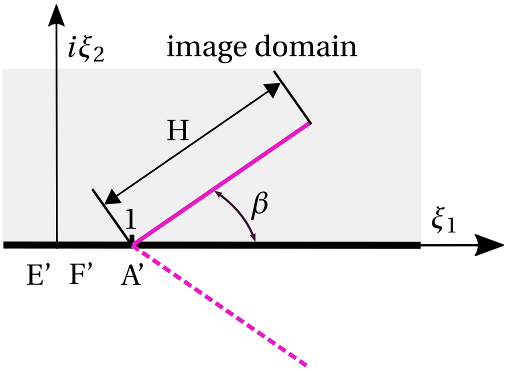

Figure 4.3: Depicted is a vorticity panel (—) and it's mirrored vorticity panel (- - -) in the image domain of the Schwarz-Christoffel mapping from Figure 4.2. The panel is a straight line from the point $\xi = 1$ with length H and angle β towards the ξ_1 axes.

in a predefined angle. The correction is applied as a tiny vorticity sheet. In the image domain, the vorticity sheet is a straight line from the point A' ($\xi = 1$) with the length H and the angle β towards the ξ_1 axes, see Figure 4.3. The angle β can be derived by evaluating the angle in the physical domain and mapping it to the image domain. It is noted that β is influenced by the flame front. For the length H, further analytical investigation is required. In this thesis, $\beta = \pi/8$ and $H = 2$ were chosen to fit the CFD simulations from Steinbacher et al. [26] with a confinement ratio of $C_r = 0.4$ and a feed duct radius of $R_i = 5\ [mm]$.
To fulfill the boundary condition that the ξ_1 axes is a streamline, the vorticity panel needs to be mirrored in the ξ_1 axes so that the induced velocity in ξ_2 direction vanishes on the ξ_1 axes, see Figure 4.3.
The integral circulation G of the orignial vorticity panel can be calculated as:

$$G = \Phi_\xi(A') \cdot \frac{i \cdot \pi}{\operatorname{atan}(\sqrt{H}) \cdot \left(e^{-i\beta} - e^{i\beta}\right)} . \tag{4.13}$$

Then the derivation $\frac{\partial \Phi_\xi}{\partial \xi}$ of the Kutta-panel yields to the expression

$$\begin{aligned} \left(\frac{\partial \Phi_\xi}{\partial \xi}\right) = & \frac{i}{\pi} \cdot \frac{G}{(\xi - 1) \cdot e^{-i\beta} + 1} \cdot \\ & \left[\operatorname{atan}(\sqrt{H}) - \sqrt{(1-\xi) \cdot e^{-i\beta}} \cdot \operatorname{atan}\left(\sqrt{\frac{H}{(1-\xi) \cdot e^{-i\beta}}}\right)\right] \cdot e^{-i\beta} . \end{aligned} \tag{4.14}$$

For the effect of the mirrored panel, only the imaginary number i in Equation (4.14) needs to be replaced with $-i$. Using the additive property of the Laplace-equation, one can evaluate the resulting velocity due to the entering velocity u_E and the vorticity panels in the physical domain as:

$$\tilde{u}_{pot}(\xi) = \sum_i \frac{\partial \Phi_{\xi,i}}{\partial \xi} \cdot \left(\frac{\partial x}{\partial \xi}\right)^{-1} . \tag{4.15}$$

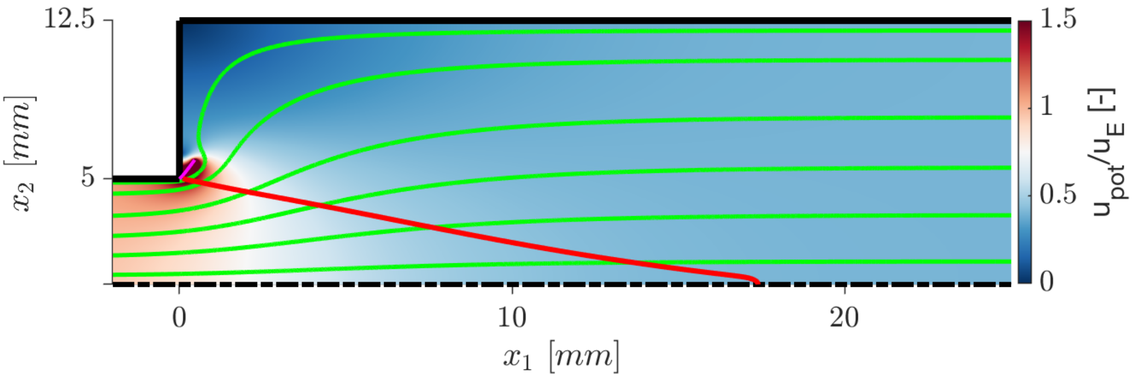

Figure 4.4: Visualization of the of the normalized acoustic velocity field in the duct geometry with a confinement ratio of $C_r = 0.4$. Also depicted are the duct walls (—), the centerline (- - -) of the duct geometry and streamlines (—) of the velocity field. A Kutta-condition is applied at the corner as a vorticity panel (—). Also can be seen a flame front (—).

The potential velocity field with the vorticity panel (—) can be seen in Figure 4.4. Comparing the streamlines with the vorticity panel (Figure 4.4), with the streamlines without any panel (Figure 4.2(a)), one can see that the panel deflects the streamlines close to the point A and bends them around the panel. Plotting the normalized flame normal velocity $u_\perp / u_E$ at the flame front of Figure 4.4 over the normalized flame aligned coordinate x_1^F / L_f, the difference becomes more obvious. The flame normal velocity without Kutta-panel (- - -) is infinitely high at the flame base, whereas the velocity with Kutta-panel (—) takes a finite value, see Figure 4.5. The influence of the Kutta-panel is only present in the vicinity of the panel and diminishes at the flame tip. Also depicted in Figure 4.5 is the result from a CFD simulation (·····) from Steinbacher et al. [26]. Up to a value of $x_1^F / L_f = 0.4$, the acoustic modeling with the Kutta-panel delivers reasonable results compared to the CFD simulation. For $x_1^F / L_f > 0.4$, the influence of the flame flow feedback towards the acoustic plays an important role as it seems to dampen the acoustics. This dampening effect can not be captured by the acoustic-modeling and yields to a higher velocity at the flame tip compared to the CFD results.

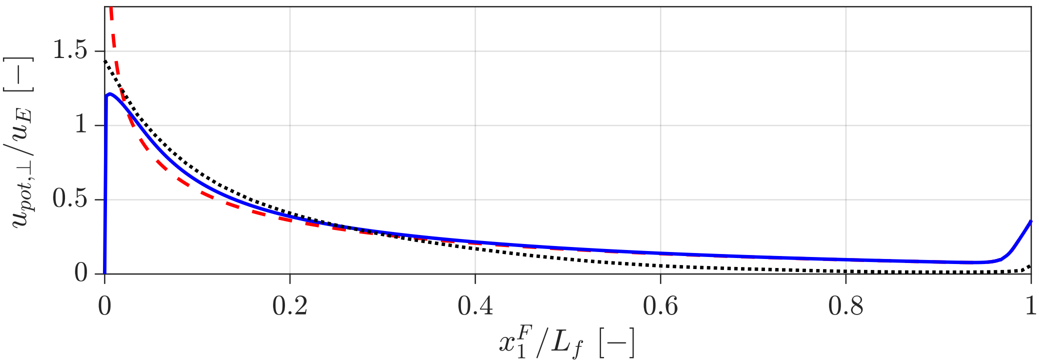

Figure 4.5: Plot of the normalized velocity $u_{pot,\perp}/u_E$ perpendicular to the flame front over the normalized flame aligned coordinate x_1^F/L_f, compare Figure 3.2. Compared are results from a CFD simulation (·····) with the results from the applied acoustic modeling with Kutta-condition (—) and without Kutta-condition (- - -). The CFD results are adopted from Steinbacher et al. [26].

5 Volume Production Modeling

In Section 2.4 it was already derived that the flame front produces volume and therefore a velocity acceleration across the flame front is induced.
The goal of this chapter is to model the volume production so that the velocity field u_{vol} is obtained. Section 5.1 explains that the volume production can be modeled by putting some sources on the flame front. In combination with the mapping, a velocity jump arises directly at the flame front with an infinitely high velocity at the source center. As this sudden velocity jump is quite unrealistic, the potential source is modified so that the volume production $\dot{V}_{p,s}$ from the potential source is distributed in space, see Section 5.2.1. The new obtained velocity field u_{vol} with the modified sources is then smoother and the singularity at the source center vanishes. It is also shown that u_{vol} correlates well with CFD simulations.

5.1 The Laplace-Source

The general formula for the volume production per unit height and unit depth along the flame front was already derived in Section 2.4, compare Equation (2.14). The volume production is continuous along the flame front and induces a velocity field $\vec{u}_{vol}$, which accelerates the fluid at the flame front (Section 2.3). This induced velocity field is irrotational and the divergence $\nabla \cdot \vec{u}_{vol} = 0$ vanishes, except at the flame front where the volume is produced [8]. Hence, $\vec{u}_{vol}$ obeys a Laplace-equation with a discontinuity at the flame front.
In this section, a discrete approximation of the volume production is derived. A couple of sources are positioned on the flame front, see Figure 5.1. Each of those sources represents a part of the flame front with the length Δs_i. The volume flux $\dot{V}_{p,s_i}$ that is produced by each source, is equal to the produced volume flux of the flame front part. With Equation (2.14), volume flux $\dot{V}_{p,s_i}$ can be expressed as:

$$\dot{V}_{p,s_i} = s_{L,u} \cdot (E-1) \cdot \Delta s_i \, . \tag{5.1}$$

Note that here the generalexpression with $s_{L,u}$ instead of $s^0_{L,u}$ is used. The higher the number of sources on the flame front, the smaller Δs_i becomes (compare Figure 5.1) and therefore, $\dot{V}_{p,s_i}$ decreases. At the same time, the volume production along the flame front becomes more continuous. For an infinite number of sources, the flame front is fully occupied and an exact volume production by the flame front is obtained. A similar approach was already demonstrated by Choi et al. [8], who used source panels to model the gas expansion induced velocity field.
For a flame front in a duct geometry, the duct walls have to be considered when evaluating

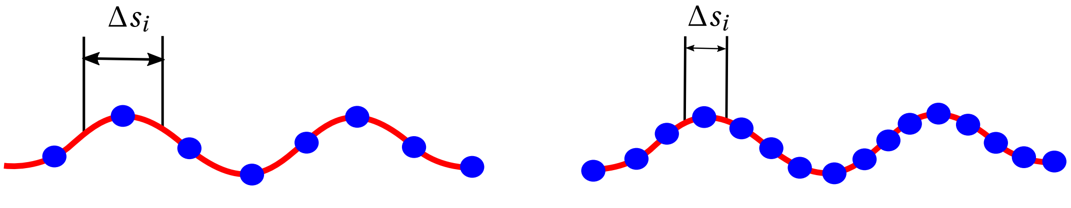

(a) (b)

Figure 5.1: Visualization of a flame front (—), which is occupied with sources (•). Each of those sources represent the volume production of the flame front length Δs_i.

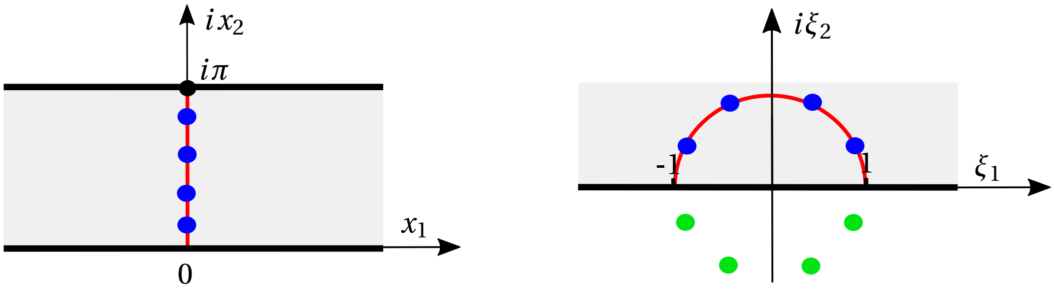

(a) physical domain (b) image domain

Figure 5.2: Visualization of a flame front (—) in a duct geometry (a), which is occupied with sources (•). Also depicted is the flame front location with the orignial (•) sources and the mirrored sources (•) in the image domain (b).

the velocity field $\vec{u}_{vol}$. As the sources fulfill the Laplace-equation a mapping can be applied, as illustrated in Chapter 4. Therefore the source location in the physical domain (•) needs to be mapped to the image domain, see Figure 5.2. To retain the boundary condition that the ξ_1 axes is a streamline, the sources has to be mirrored (•) at the ξ_1 axes, compare Figure 5.2. The resulting velocity field induced by the modeled gas expansion can then be evaluated in the physical domain according to Equation (4.15) and Equation (4.5). This is plotted in Figure 5.3. For an unstretched flame front, u_{vol} vanishes in the unburnt gas. This is due to the fact that $x_1 = -\infty$ reduces in the image domain to a single point ($\xi = 0$). As the sources and the mirrored sources build a closed geometry around the origin in the image domain (Figure 5.2(b)), no volume flux can stream towards $\xi = 0$ and hence, towards $x_1 = -\infty$ in the physical domain. Adding a sink at $\xi = 0$, would lead to the volume produced by the sources being absorbed and therefore a stream towards $x_1 = -\infty$ could arise.

As it can be seen in Figure 5.3, the induced velocity u_{vol} jumps across the flame front according to Equation (2.8). The discontinuity in the potential Φ at the flame front leads to an infinitely high velocity at the source location. Thus, the obtained velocity field u_{vol} can not be used with the G-equation to model the flame front motion and would need a correction term. In this thesis, a similar modeling approach with a modified source is used, see Section 5.2.

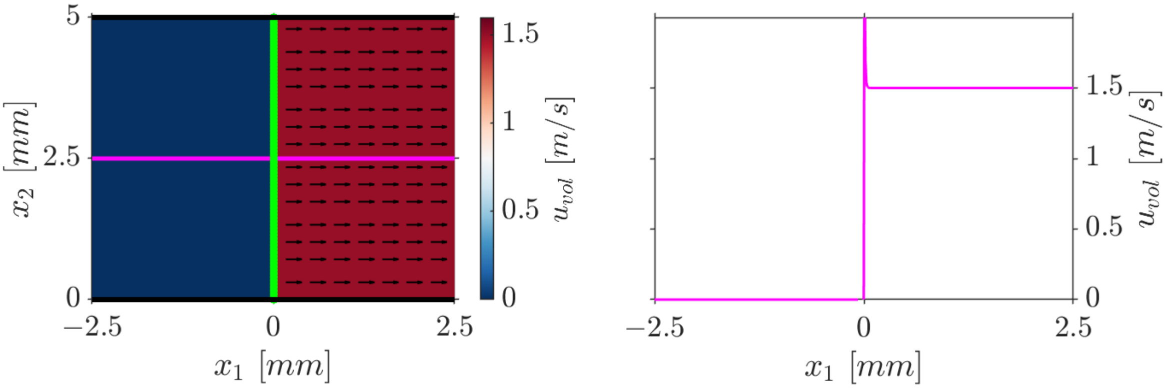

Figure 5.3: Plot of the velocity field in a duct geometry (a), which is induced by the potential sources (—). The sources are located on the vertical line at $x = 0$. The velocity on the horizontal line (—) is depicted in (b). The result was obtained with a burning velocity $s_L^0 = 0.25$ [m/s], an expansion ratio of $E = 7$ and 250 sources.

5.2 The Desingularized-Source

The main problem using the classic potential source for modeling the gas expansion induced velocity field u_{vol}, is the discontinuity in volume production. All the volume flux $\dot{V}_{p,s_i}$ is produced in a single point at the source center. This yields to a sudden velocity jump with an infinitely high velocity at the flame front position, compare Figure 5.3. Furthermore, the velocity jump is quite unrealistic, especially when simulating a flame front with a length in the range of millimeters. In this case, a smoother velocity profile is expected, similar to the temperature profile from Figure 2.2.

In this section, a modified source is presented. First, the characteristics of the new source are discussed. It is then explained that the obtained velocity profile through the flame front yields to another interpretation of the G-equation than previously illustrated in Section 3.1. Finally, it is discussed how many sources are needed for a precise simulation of u_{vol}.

5.2.1 Characteristics

To correct the modeling with the potential source, a modified source is introduced.This is in the following called the desingularized source. The velocity induced by a single desingularized source is:

$$u_{vol,r} = \underbrace{\frac{\dot{V}_{p,s_i}}{2 \cdot \pi \cdot r}}_{\text{potential source}} \cdot \underbrace{\left[1 - exp\left(-\frac{r^2}{(r_0/2)^2}\right)\right]}_{\text{additional term}} . \tag{5.2}$$

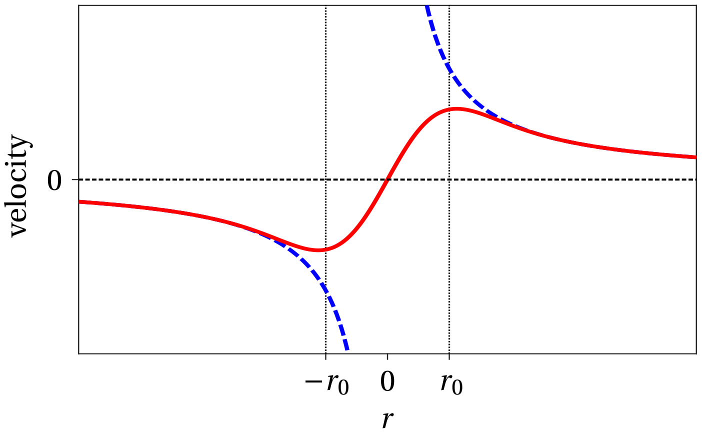

Figure 5.4: Plot of the velocity profiles of the desingularized source (—) and the potential source (- - -) over the radial coordinate r.

Here, the velocity was expressed in cylindrical coordinates and the subscript $(\cdot)_r$ denotes the radial direction. Note the similarity to the expression for the Lamb-Oseen Vortex. The first term on the right hand side of Equation (5.2) is equal to the velocity field induced by the potential source. The second term is an additional correction term, dependent on the source radius r_0. The influence of r_0 on u_{vol} is discussed later.

A comparison between the velocity induced by a potential source (- - -) and the desingularized source (—) can be seen in Figure 5.4. It is apparent that the correction term only influences the velocity in the vicinity of the source center ($r < r_0$), where it changes the singularity from the potential source. For $r > r_0$, both velocities profiles are approaching as the value of the exponential term decreases for an increasing r.

As the desingularized source only induces a velocity in radial direction, the curl $\nabla \times \vec{u}_{vol} = 0$ vanishes. Hence, the resulting velocity field is irrotational, as was already the case for the potential source. For the divergence $\nabla \cdot \vec{u}_{vol}$, the following expression in cylindrical coordinates is obtained:

$$\nabla \cdot \vec{u}_{vol} = \frac{\dot{V}_{p,s_i}}{\pi \cdot (r_0/2)^2} \cdot exp\left(-\frac{r^2}{(r_0/2)^2}\right). \tag{5.3}$$

The above equation exhibits that the singular volume production of the potential source is distributed in space by an expression, similar to the Gaussian-kernel (Equation (3.19)). A volume production comparison between the potential source and the desingularized source can be seen in Figure 5.5. The main volume production of the source takes place inside the radius r_0 and the total amount of produced volume is $\dot{V}_{p,s_i}$.

To model the gas expansion induced velocity field u_{vol}, the same technique with the mapping from Section 5.1 is applied.

First, the sources are placed on the flame front and are then mapped to the image domain. In the image domain, they need to be mirrored at the ξ_1 axes and then the resulting velocity field can be calculated with Equation (4.15). The complex derivation of the potential Φ_ξ of a single

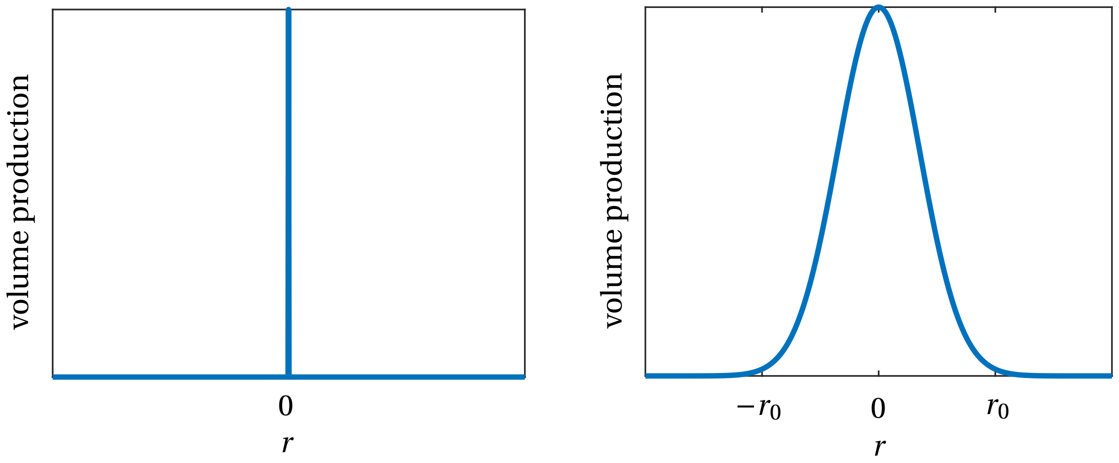

(a) potential source

(b) desingularized source

Figure 5.5: Plot of the volume production profiles of the potential source (a) and the desingularized source (b) in cylindrical coordinates over the radial coordinate r.

desingularized source is:

$$\frac{\partial \Phi_\xi}{\partial \xi} = \frac{\dot{V}_{p,s_i}}{2 \cdot \pi \cdot (\xi - \xi_s)} \cdot \left[1 - exp\left(- \frac{(\xi - \xi_s)^2}{(r_{0,\xi}/2)^2} \right) \right] . \tag{5.4}$$

Here, ξ_s expresses the position of the source. The volume strength of the source is equal to the volume strength of the potential source and can be evaluated with Equation (5.1). Special attention should be given to the length r_0, which changes when the source is mapped. The relation between r_0 and $r_{0,\xi}$ is:

$$r_{0,\xi} = r_0 \cdot \left(\frac{\partial x}{\partial \xi}(\xi_s) \right)^{-1} . \tag{5.5}$$

The resulting velocity field u_{vol}, induced by the desingularized sources, can be seen in Figure 5.6. A bulk flow equal to the unstretched unburnt laminar burning speed $s^0_{L,u}$ was added to the velocity. As it was already the case for the potential sources, the velocity in the unburnt gas is not altered by the sources. The velocity acceleration through the flame front is now smoother and the main acceleration begins at $x_1 = -r_0$ and ends at $x_1 = r_0$, compare Figure 5.6(b). As a comparison, a velocity profile from a Cantera simulation, produced by Steinbacher [23], is plotted. The parameter r_0 was adjusted to fit the velocity profile. In general, r_0 should be half the flame thickness. It can be seen that the modeled velocity profile with the desingularized sources (—) matches the Cantera velocity profile (- - -). Only at the end of the flame front, the velocity profiles differ.

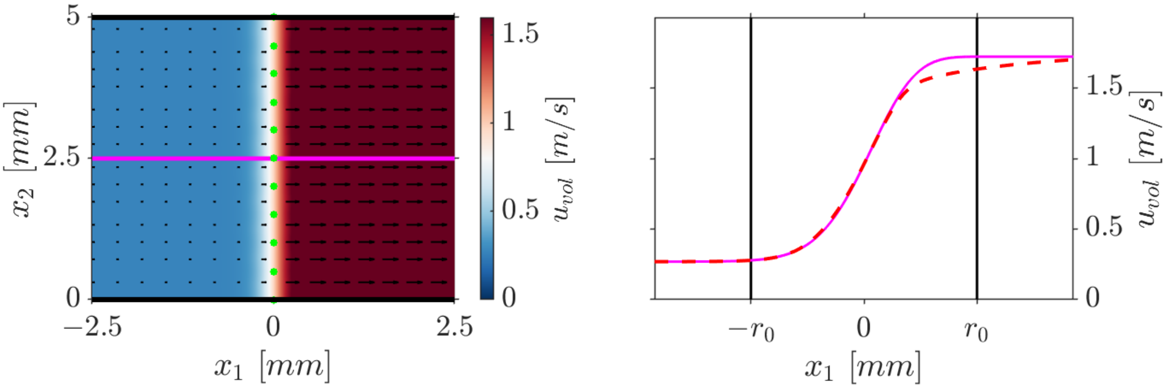

Figure 5.6: Plot of the velocity field in a duct geometry (a), which is induced by the desingularized sources and a bulk flow. The sources (●) are located at the vertical line at $x = 0$. The velocity on the horizontal line (—) is depicted in (b). Also shown is the velocity profile from a Cantera simulation (- - -) (GRI 3.0 mechanism), produced by Steinbacher [23]. To fit the velocity profile from the Cantera Simulation, the parameters $u_{bulk} = s_L^0 = 0.269$ $[m/s]$, $E = 6.4$ and $r_0 = 0.53$ $[mm]$ were used. The number of sources is only 11.

5.2.2 G-Equation Solver Coupling

In Section 3.1, the G-equation was introduced. It was explained that the G-equation can be understood as an infinitely thin surface, separating the unburnt gas and the burnt gas. This surface moves according to the gas velocity u and the burning velocity s_L.

In contrast to that, the modeled velocity field with the desingularized sources does not naturally feature this infinitely thin flame front property any more. The gas is now accelerating through a flame front with a defined thickness. The question arises which velocity should now affect the $G = 0$ isoline, modeled with the G-equation. This leads to another interpretation of this infinite surface. The flame front is now modeled as a sheet, consisting of several infinitely thin surfaces, compare Figure 5.7(a). All those surfaces are parallel to each other and move with another burning velocity s_L. The sources are placed on the surface (—) which is located in the center of the flame front, see Figure 5.7(a). The first of those surfaces (—) represents the beginning of the flame front and moves with the laminar burning velocity $s_{L,u}$. It's distance from the sources is r_0 and therefore, the velocity u is not affected for an unstretched flame front, compare Figure 5.7(b). The last of those surfaces (—) represents the end of the flame front and is positioned at a distance r_0 from the sources, moving with the burning velocity $s_{L,b}$. As $s_{L,b} > s_{L,u}$, this surface moves faster relative to the unburnt gas. In contrast to that, the velocity u is also higher at the surface, keeping both surfaces parallel. In general one could define the $G = 0$ isoline towards any thin surface in the flame front. As the surfaces are described by the $G = 0$ isoline, they are referred as isolines in the following.

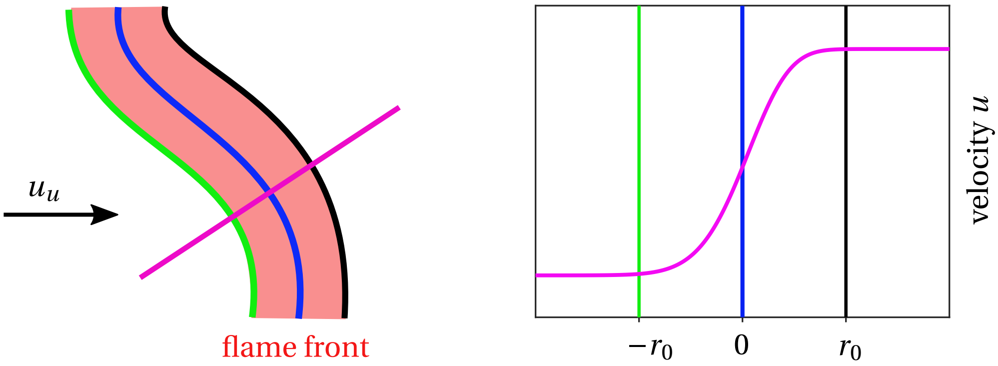

(a) (b)

Figure 5.7: Schematic representation of a thick flame front (🟥) with several isolines (a). Due to the gas expansion, the velocity (—) increases through the flame front (b). Hence, the different isolines are affected by a different velocity u. The different isolines and their corresponding position in the velocity plot are depicted in the same color.

5.2.3 Required Number of Sources

Even though the volume production is distributed in space with the desingularized source, it is still not totally continuous along the flame front. Hence, the question arises how many sources should be positioned on the flame front for an appropriate simulation of u_{vol}?
With an increasing amount of sources, the volume production along the flame front get's more continuous. A plot of the volume production by several sources on a line can be seen in Figure 5.8. In general, the amount of sources needed depends on the flame length L_f and the radius r_0, see Figure 5.9 (a). For an increasing flame length, more sources are needed to occupy the flame front. With an increasing value r_0, the area where the volume is produced, increases. This leads to an overlap of the volume production areas and therefore the volume production gets more continuous, compare Figure 5.8 (a)-(c).
A simple investigation can be made by putting several sources on the line (—) and then evaluating the induced velocity at different areas. Here, these different areas are two lines parallel to the source line in a distance of $-r_0$ (—) and r_0 (—), compare Figure 5.9 (a). Additionally, the velocity is evaluated directly at the source line. With an increasing number of sources, the induced velocity will converge to a specific value u_{ref} at each line and the difference in the velocity along the line vanishes. A plot of the non-dimensional velocity difference $\Delta u^* = (u - u_{ref})/u_{ref}$ over the non-dimensional source number $n^* = (N \cdot r_0)/L_f$ can be seen in Figure 5.9 (b). Here, N is the number of sources. For Δu^*, the maximum value along the line is plotted. It can be seen that for a value of $n^* = 1$, the maximum relative discrepancy is smaller than 5 % and for $n^* = 2$ smaller than 0.1 %. This means for an number of $n^* > 2$, no improvement in u_{vol} is obtained by increasing the number of sources on that straight line. It should be noted that especially for curved lines, the required number of sources should be

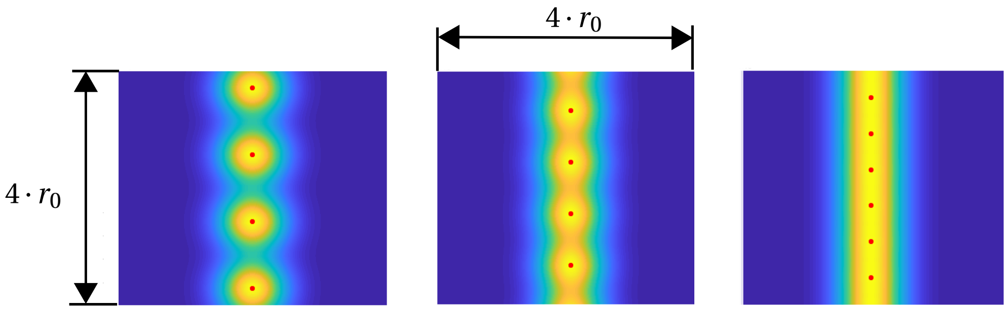

(a) (b) (c)

Figure 5.8: Comparison of the volume production with a different number of sources along a line. The brighter the area, the more volume is produced. In all three images, the investigated domain is a square of $4 \cdot r_0$ side length. To illustrate the source position, the source center (•) is plotted.

higher to capture the impacof the flame front curvature on the velocity field u_{vol}.

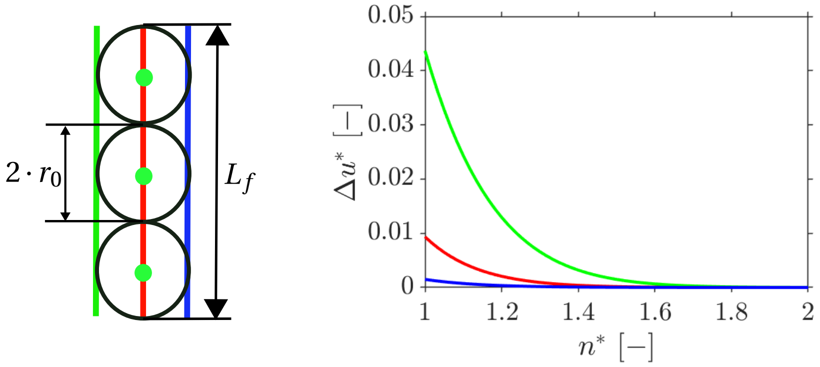

(a) (b)

Figure 5.9: In (a), several sources are positioned on the line (—) with the length L_f. The induced velocity is then evaluated along the three different colored lines. In (b), the relative velocity $\Delta u^* = (u - u_{ref})/u_{ref}$ is plotted over the non-dimensional number of sources $n^* = (N \cdot r_0)/L_f$. For Δu^*, the maximum value along each line is plotted. To obtain the value u_{ref}, a number of $n^* = 100$ sources was taken.

6 Impact of the Gas Expansion on the Flame Shape

After deriving the model for the gas expansion induced velocity field u_{vol} in Chapter 5, the impact on the flame shape is discussed in this chapter. The flame shapes in a simple duct geometry with and without u_{vol} are compared in Section 6.1. To categorize the influence on a real flame shape, results from a CFD simulation produced by Steinbacher [23] are shown. Afterwards the impact of several influencing parameters, for example the Markstein number Ma, are illustrated in Section 6.2. Section 6.3 goes on to present several flame shapes in a duct with a backward-facing step. This subsequently leads to an additional influencing parameter on the flame shape, the confinement ratio C_r.

6.1 Flame Shape Comparison

To simulate the flame shapes, a G-equation solver from Steinbacher [24] is used. Details about solver can be seen in [6]. This solver is supplemented by the modeled velocity field $u = u_{bulk} + u_{vol} + u'_{ac}$. The bulk flow u_{bulk} is simplified as a potential flow and can be calculated as shown in Chapter 4. The flames burn in a simple duct with a diameter $D = 2\ [mm]$. The inlet velocity in the duct is $u_E = 1\ [m/s]$ and the flames are anchored at the top at $x_1 = 0$, see Figure 6.1. The perfectly premixed gas is a methane-air mixture with an equivalence ratio of $\Phi = 0.8$, an inlet temperature of $T_u = 300\ [K]$ and a pressure of $p_u = 101325\ [Pa]$. The resulting unburnt burning velocity is $s^0_{L,u} \approx 0.26\ [m/s]$. As $u > s^0_{L,u}$ the flame front adjusts to an angle so that $u_\perp = s_{L,u}$. For the flame front simulation without gas expansion ($u_{vol} = 0$), the gas velocity $u = const.$ along the flame front. Hence, the flame angle towards the horizontal line $\alpha = const.$. The resulting flame front is a straight line (·····) with $\alpha = \sin^{-1}(s^0_{L,u}/u)$, see Figure 6.1. Compared to the CFD result (—), only the flame length is similar. Neither the convex (towards the unburnt gas) flame shape at the anchor point nor the concave flame shape at the flame tip can be predicted without the flame-flow feedback.

For the gas expansion modeling, the desingularized sources were positioned on the flame front. The resulting flame shape (- - -) with u_{vol} is depicted in Figure 6.1. It can be seen that u_{vol} alters the flame front shape as it is not constant along the flame front, compare Figure 6.2. The induced velocity is higher at the flame tip than at the flame base and hence the angle α is smaller at the flame tip. Compared to the CFD simulation, both the convex part and the concave part are more curved. It can also be seen that the flame angle in the middle of the flame front is the same for the CFD results and the G-equation results with u_{vol}. This aligns with the results from Choi and Shin [8] who said that the gas expansion increases the flame front

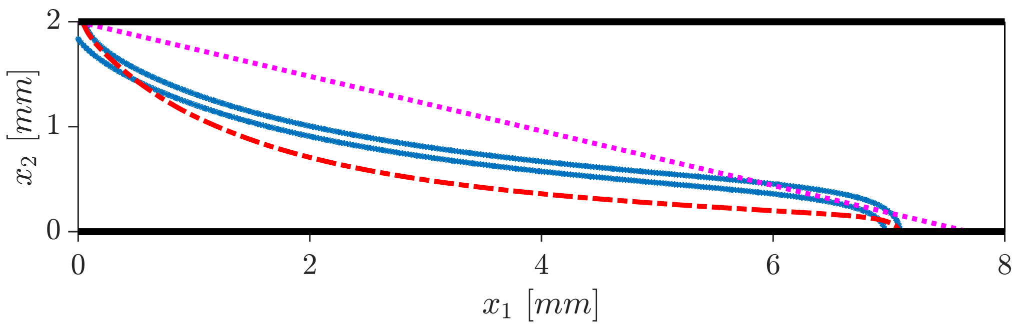

Figure 6.1: Flame shape comparison between a CFD simulation (—) from Steinbacher [23], the results of the G-equation solver with (- - -) and without the gas expansion (· · · · ·). All flames are depicted in a duct geometry (—). The parameters used for the simulation are: $u_E = 1$ [m/s]; $s_{L,u} = 0.26$ [m/s]; $s_{L,u} = 0.26$ [m/s]; $r_0 = 0.5$ [mm]; $E = 6.8$; number of sources $N = 150$ ($\widehat{=}\ n^* = 9.5$). The sources were positioned on the flame front.

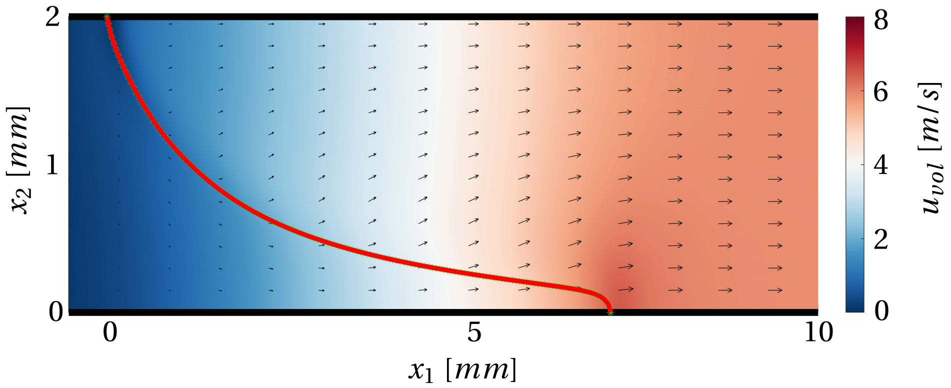

Figure 6.2: Plot of the gas expansion induced velocity field u_{vol} in a duct. The arrows denote the flow direction. The desingularized sources were put on the flame front (—). The parameters used for the gas expansion modeling are equal to Figure 6.1.

curvature whereas the barocline vorticity tends to counteract that especially in the curved areas.

6.2 Parameter Study

The flame front shape from Figure 6.1 is obtained by solving the G-equation (Equation (3.1)) which depends on two parameters, the burning velocity s_L and the gas velocity u. The burning velocity itself depends on the Markstein length which is normally adjusted in the range of the flame thickness ($\delta_M \approx \delta_F$). For the modeled velocity field u, the source radius r_0 is of importance. r_0 is also linked to the flame thickness ($r_0 \approx \delta_F/2$), compare Figure 5.6. In addition, both s_L and u depend on which isoline from the flame front is simulated, see Figure 5.7.

First, the impact of the Markstein length towards the flame shape is investigated. For a simplified interpretation, the Markstein length δ_M is non-dimensionalized as the Markstein number Ma. As explained in Section 2.2, s_L decreases at a convex (towards the unburnt gas) part of the flame front and increases before a concave part. This variation in s_L counteracts the curvature of the flame front. The strength of the counteracting effect depends on the Markstein number. Thus, for a higher Markstein number a less curved flame front is expected. This can also be observed in the flame shape simulations, see Figure 6.3. The flame front with a Markstein number Ma = 1.2 (- - -) is less curved than a flame front with Ma = 0.8 (—). The differences between those two flame shapes are most pronounced at the flame tip where the largest curvature appears. The flame with Ma = 1.2 has a bigger radius than the flame with Ma = 0.8 so s_L becomes equal for both flames. Hence, the Markstein number increases the flame tip surface and therefore the amount of gas which can be burned. This leads to a decrease in flame length, compare Figure 6.3.

For the parameter r_0, a similar behavior as for the Markstein number is expected. The higher r_0 is, the more distributed the volume production is in space and therefore the differences in u along the flame front decrease, compare Section 7.3. The closer the value of u, the smaller the curvature of the flame front, see Section 7.3. In contrast to the Markstein length, s_L is not affected and hence the flame tip curvature is only slightly altered. A comparison between two flames shapes with a different source radius r_0 is depicted in Figure 6.3.

When simulating different isolines, different flame shapes are expected. All of the isolines are parallel to each other in a real flame front and so the curvature is pronounced differently, compare Figure 5.7 (a). A concave (towards the unburnt gas) curvature is bigger at the isoline close to the unburnt gas than at the isoline close to the burnt gas. The opposite is the case for a convex curvature. Hence, the curvature κ_{curv} at the flame tip is biggest at the isoline close to the unburnt gas, compare Figure 6.4. In contrast to that, the burning velocity $s_{L,b} > s_{L,u}$. This means that even though the curvature is smaller in the burnt gas, the change in burning velocity relative to the bulk flow $(s_L - s_L^0)/u_{bulk}$ is large. Hence, the flame shape of the isoline close to the burnt gas is more sensitive to a changing Markstein number than the isoline close to the unburnt gas. In general, the Markstein number Ma is smaller for the isoline close to the burnt gas than for the isoline close to the unburnt gas [10]. This is shown in Figure 6.4, where a higher Markstein number Ma = 1.2 was chosen for all isolines compared to Figure 6.1. It can be seen that the isoline close to the burnt gas is way shorter than the isoline close to the unburnt gas. It is also questionable how the effect of barocline vorticity affects the different isolines.

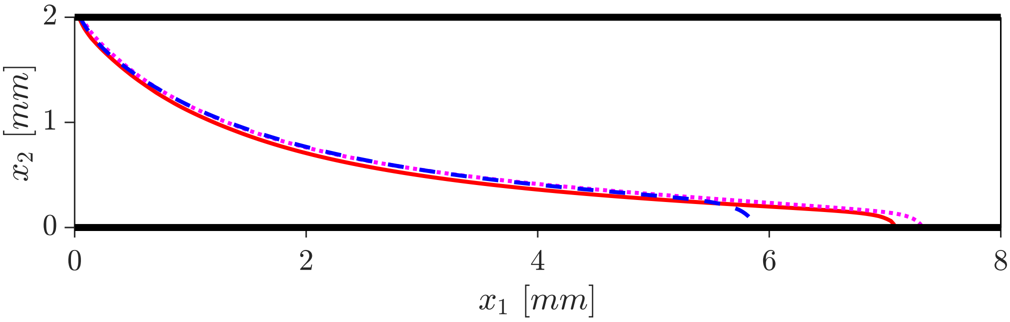

Figure 6.3: Depicted is a flame front in a duct geometry (—) modeled with the gas expansion effect and the G-equation solver (—). The parameters used are: $u_E = 1$ $[m/s]$; $s_{L,u} = 0.26$ $[m/s]$; Ma=0.8; $r_0 = 0.5$ $[mm]$; $E = 6.8$; $N = 150$ ($\widehat{=}$ $n^* = 9.5$). Also shown is a flame front with Ma=1.2 (- - -) and a flame front with $r_0 = 1$ $[mm]$ (·····). The sources were positioned on the flame front.

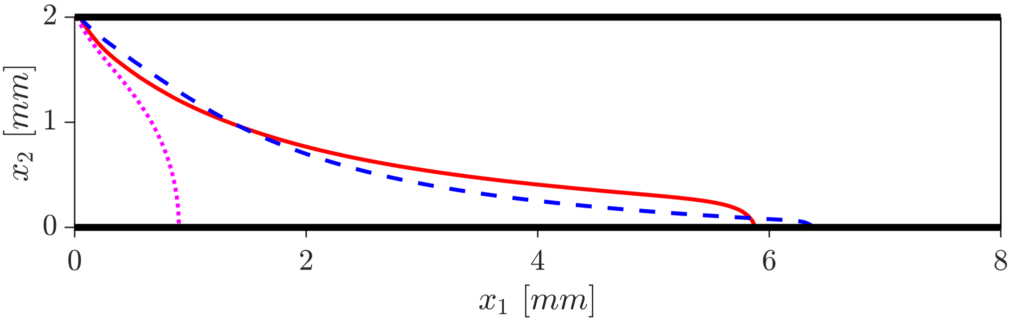

Figure 6.4: Depicted are three flame fronts in a duct geometry (—) modeled with the gas expansion effect and the G-equation solver. The difference between the simulations is the source position: sources before the flame front at a distance r_0 (·····); sources on the flame front (—); sources behind the flame front at a distance r_0 (- - -). The parameters used for the simulations are: $u_E = 1$ $[m/s]$; $s_{L,u} = 0.26$ $[m/s]$; Ma=1.2; $r_0 = 0.5$ $[mm]$; $E = 6.8$; $N = 150$ ($\widehat{=}$ $n^* = 9.5$).

6.3 Impact of the Duct Geometry on the Flame Shape

After analyzing the impact of several flame front parameters on the flame shape in Section 6.2, Section 6.3 goes on investigating the influence of the duct geometry. Therefore the backward-facing step duct from Section 4.2.2 is used. The potential bulk flow u_{bulk} differs compared to the simple duct geometry, with reference to Section 4.2. In the axial direction, $u_{bulk,1}$ is decelerated by virtue of the step. In contrast to that an additional velocity term $u_{bulk,2}$ in radial direction arises in the vicinity of the step, compare Figure 4.4. That leads to a bulk flow which is no more constant along the flame front. The resulting flame shape (·····) only simulated with u_{bulk} can be seen in Figure 6.5. Compared to the straight line velocity shape from Section 6.1, the flame becomes shorter as $u_{bulk,1}$ is decreased. However the flame curvature is

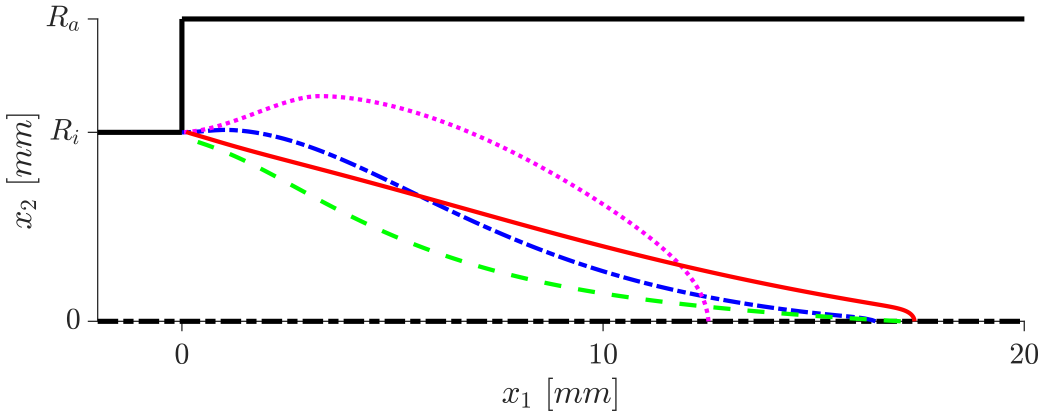

Figure 6.5: Flame shape comparison in a duct (—) with a backward-facing step. Depicted is a flame front simulated with (-·-) and without (·····) the gas expansion effect u_{vol}. Both are compared to a CFD simulation result (—) from Steinbacher et al. [26]. All three flames burn in a duct with a confinement ratio of $Cr = R_i/R_a = 0.4$. The parameters used are: $R_i = 5\ [mm]$; $u_E = 1\ [m/s]$; $r_0 = 0.5\ [mm]$; $E = 6.8$; Ma=1; $N = 150$ ($\widehat{=}\ n^* = 9.5$). In addition to that, a flame front simulated with u_{vol} in a duct and a confinement ratio of $Cr = 0.66$ (- - -) is shown.

highly increased due to the $u_{bulk,2}$ component. As it was already the case in Section 6.1, the gas expansion u_{vol} induces a high velocity at the flame tip leading to a more concave flame front (-·-), compare Figure 6.6. In Figure 6.7, it can be seen that the streamlines are first deflected towards the center line before passing the flame front. This is particularly noticeable at the flame center. With an increasing confinement ratio $C_r = R_i/R_a$, the space in the radial direction for the gas to expand decreases. Thus, the radial velocity u_{x_2} decreases. The flame shape then becomes more concave, especially at the flame base. This effect can be seen in Figure 6.5 when comparing the flame shape with $C_r = 0.4$ (-·-) and $C_r = 0.66$ (- - -). For $C_r = 1$ the flame shapes from Section 6.1 are reproduced.

Compared to the CFD results from Steinbacher et al. [26], the simulated flame shapes are more curved. This can be once again explained due to the missing effect of barocline vorticity which counteracts the curvature [8].

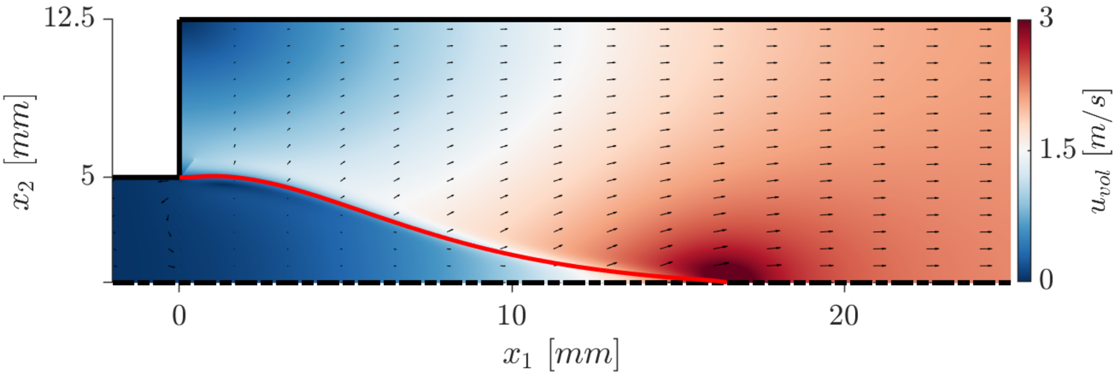

Figure 6.6: Depicted is the induced velocity u_{vol} by the flame front in a duct (—) with a backward facing step. The flame front (—) corresponds to the flame front (- - -) from Figure 6.5.

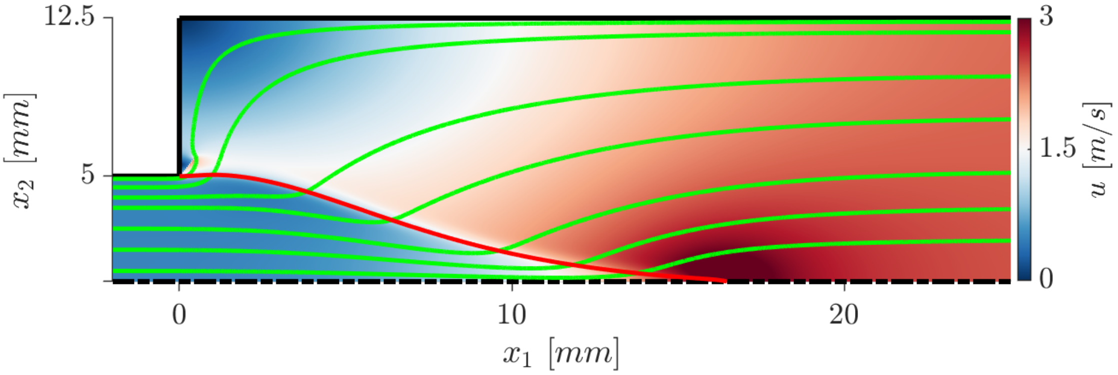

Figure 6.7: Depicted is the velocity field $u = u_{bulk} + u_{vol}$ in a duct (—) with a backward facing step. The flame front (—) corresponds to the flame front (- - -) from Figure 6.5. Also shown are streamlines (—).

7 Impact of the Gas Expansion on the FTF

The influence of the gas expansion on the flame shape is discussed in Chapter 6. It is shown that the gas expansion increases the curvature of the steady state flame shape. However, one also needs to account for the effect of barocline vorticity production along the flame front to accurately predict the flame shape. While often precluding from the influence of the gas expansion, existing literature proves the importance of the barocline vorticity for the FTF With the derived model in Chapter 5, a systematic investigation of the impact of gas expansion on the FTF can be done. Previously, the G-equation solver [24] is validated in Section 7.1. This is done with the convective incompressible velocity model with Gaussian-kernel (CIG-model), presented in Section 3.3.2. Afterwards, a first comparison between the G-equation solver results and CFD results from Steinbacher et al. [26] is made in Section 7.2. Section 7.3 investigates the influence of several parameters on the FTF. The chapter finishes by investigating the impact of gas expansion on the convective waves and the Darrius-Landau mechanism.

7.1 Solver Validation

To validate the G-equation solver [24], a short FTF comparison between the theoretical prediction with the CIG-model and the solver results with the CIG-model is made. For the solver, a constant burning velocity s_L^0 is assumed. The bulk flow assumes a jet flow with $u_{bulk} = 1\ [m/s]$ and the distortions travel with the bulk flow speed ($K = 1$). The kernel width for both, the solver and the theoretical model, was chosen as $\sigma = 2.3\ [ms]$. The resulting flame transfer functions are depicted in Figure 7.1. It can be seen that both, the IR and the FR, show a very good alignement for the solver (- - -) and the theoretical model (—). It is noted that the characteristic timescale τ_r was increased for the solver so that both IRs start to oscillate at the same time t^*. The reason for that is that the theoretical model seems to alter the timescale τ_r, compare Section 3.3. Overall, the solver delivers reasonable results for the following FTF analysis.

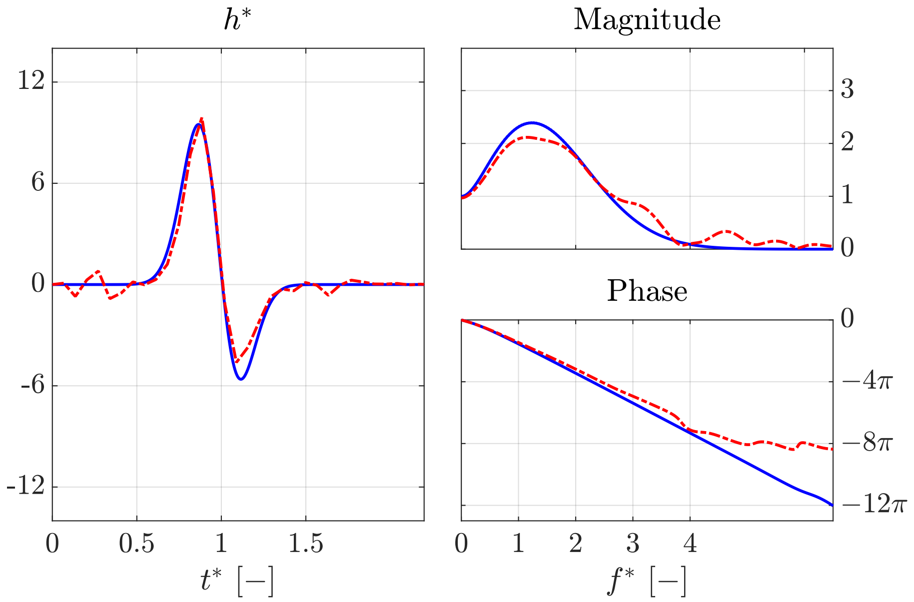

Figure 7.1: Comparison of the FTF between the theoretical GIC model (—) and the G-equation solver result (- - -) based on GIC velocity model. The parameters used are: $\sigma = 2.3$ $[ms]$; $K = 1$; solver: $\tau_r = 18.7$ $[ms]$; theoretical model: $\tau_r = 21$ $[ms]$

7.2 FTF Comparison

When analyzing the acoustic based velocity models for the FTF in Section 3.3.1, it was shown that an acoustic perturbation alone can not explain the oscillating IR and the high magnitude in the FR of the CFD FTF. The same conclusions result from the G-equation solver simulations. When neglecting the gas expansion induced velocity field u_{vol}, the resulting FTF (·····) does not feature the oscillation in the IR, see Figure 7.2. It is noted that the bulk flow was modeled as a jet for the simulation without u_{vol}, to obtain a more similar flame shape compared to the CFD simulation, compare Figure 6.5. Also a higher timescale τ_r can be observed due to the lower bulk flow. The FTF with the modeled velocity field u_{vol} (- - -) obtains both, the oscillation in the IR and the high magnitude in the FR. Hence, the effect of the gas expansion is linked to the oscillation and the high gain.

Compared to the CFD simulation (—), the first high peak in the IR is not captured in the G-equation solver result. This is explained by the different flame shapes, compare Figure 6.5. The disparity in flame angle at the flame base leads to a different normal acoustic velocity perturbation $u'_{ac,\perp}$ at the flame front Figure 7.3. The perturbation at the flame base of the G-equation solver flame shape is about half the perturbation of the CFD flame shape. Hence, the IR of the CFD simulation is higher as well. In addition to that, the timescale τ_r is reduced due to the shorter flame length. Despite this, both IR oscillate with a similar frequency. The small difference in the oscillation frequency vanishes when adjusting the influencing parameters.

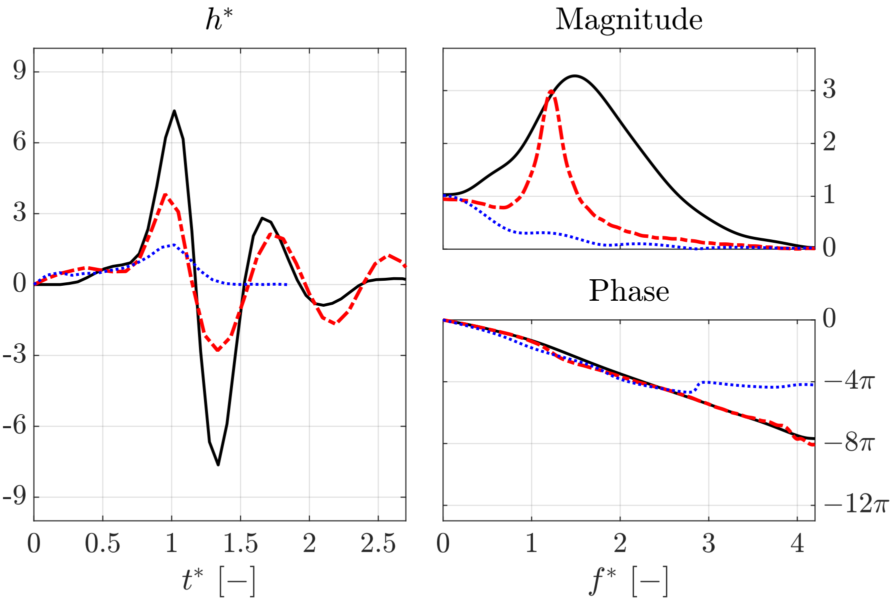

Figure 7.2: Comparison of the FTF between the G-equation solver results and the CFD simulation results (—) ($\tau_r = 15.7$ [ms]) from Steinbacher et al. [26]. For the G-equation solver results two different FTF are depicted, one simulated with the gas expansion induced velocity field (- · -) ($\tau_r = 15$ [ms]) and one without it (· · · · ·) ($\tau_r = 18$ [ms]). With the exception of the Markstein number, which was chosen as $Ma = 0.3$ for both G-equation solver results, the parameters used correspond to the parameters from Figure 6.5.

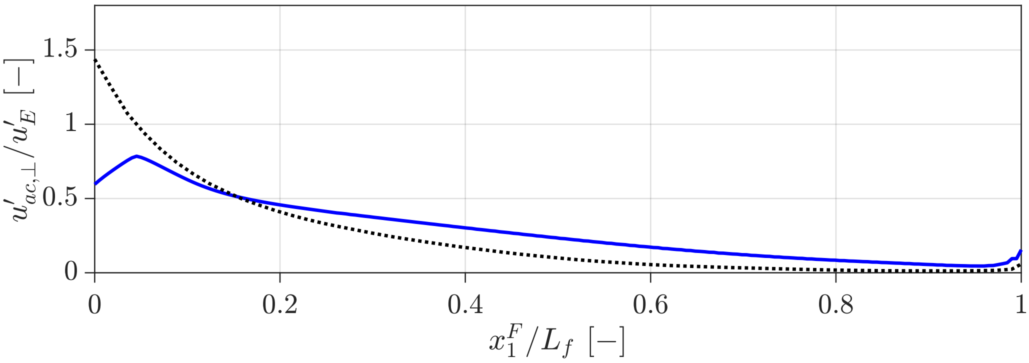

Figure 7.3: Plot of the normalized acoustic velocity perturbation $u'_{ac,\perp}/u'_E$ perpendicular to the flame front over the normalized flame aligned coordinate x_1^F/L_f, compare Figure 3.2. Compared are results from a CFD simulation (· · · · ·) with the results from the applied acoustic modeling with Kutta-condition (—). The flame shapes used to evaluate the normal velocity correspond to Figure 6.5 with a confinement ratio of $C_r = 0.4$.

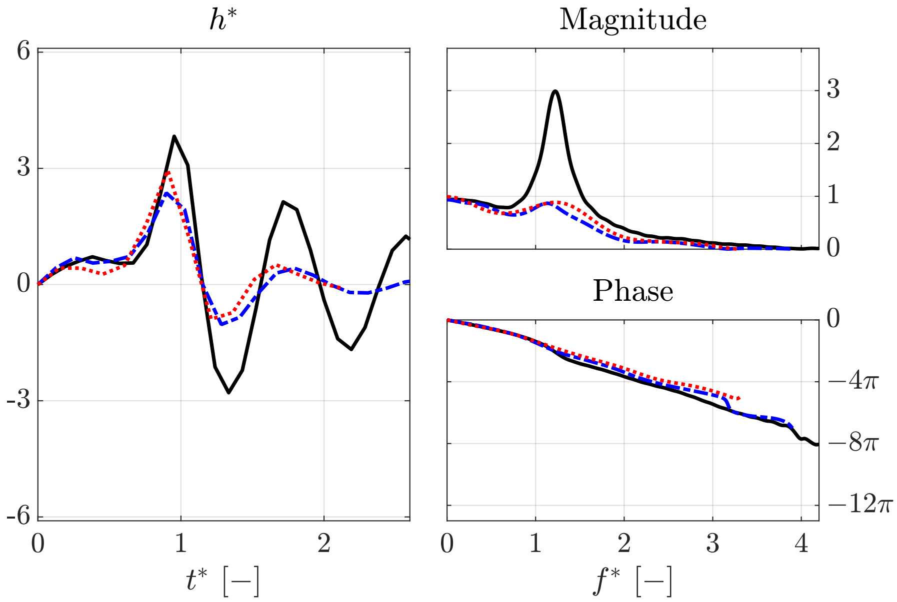

Figure 7.4: Comparison of three different FTF modeled with the impact of the gas expansion. As reference simulation (—) (Ma = 0.3; $r_0 = 0.5$ $[mm]$; $\tau_r = 15$ $[ms]$) serves the FTF from Figure 7.2. Also depicted is a FTF with an increased Markstein number (·····) ($\tau_r = 11.8$ $[ms]$; Ma = 1) and an increased source radius (- - -) ($\tau_r = 15.7$ $[ms]$; $r_0 = 1$ $[mm]$).

7.3 Parameter Study

In Chapter 6 the impact of several parameters on the flame shape was investigated. These parameters are: the Markstein number Ma, the source radius r_0 and the confinement ratio C_r of the duct geometry. It was found that all of them influence the FTF. Thus, a concise parameter study is done in this section.

First, the impact of the Markstein number is analyzed. When a disturbance travels along the flame front, it can either be increased or decreased, depending on the growth rate σ_g. The latter is negatively correlated with the value of the Markstein number, with reference to Section 2.7. Hence, a higher Markstein number suggests a damping effect on the IR. This becomes evident, when comparing the FTF with Ma = 0.3 (—) and Ma = 1 (·····), see Figure 7.4. Especially the second and the third oscillation peaks are highly damped. The first peak, however, is only slightly decreased. This can be explained by the higher flame normal acoustic perturbation resulting from a less curved flame shape as Ma increases, compare Section 7.2. A damped IR corresponds to a decreased magnitude in the FR. The oscillation frequency of the IR increases with increasing Markstein number, whereas the timescale τ_r is reduced. To explain both effects, further investigation is required.

For an increasing source radius (- - -), a similar behavior can be observed. The IR is damped, leading to a lower magnitude in the FR. The explanation for that is that the volume production is more distributed in space and hence gradients in the velocity u decrease. Hence, the growth

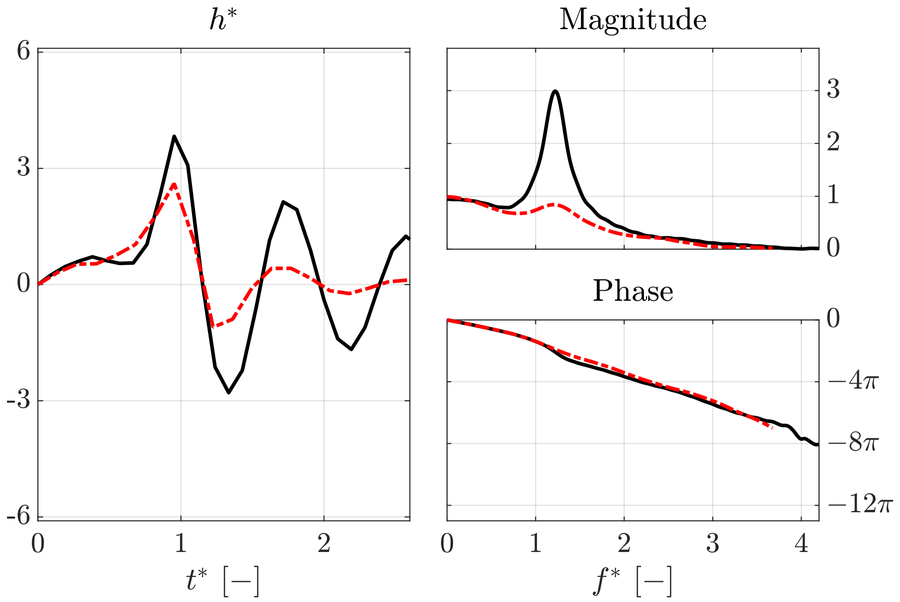

Figure 7.5: Comparison of two FTFs modeled with the impact of the gas expansion. These FTF are obtained with the parameters from Figure 7.2. The only variation is the confinement ratio C_r which is $C_r = 0.4$ (—)($\tau_r = 15$ $[ms]$) and $C_r = 0.66$ (- - -) ($\tau_r = 10.5$ $[ms]$) .

rate σ_g declines, compare Section 2.7. In contrast to the impact of the Markstein number, the oscillation frequency of the IR decreases. The timescale τ_r is only slightly increased by the source radius. This may be explained with an increased flame length, compare Figure 6.3.
The confinement ratio C_r influences the flame base distortion. The flame base angle towards the horizontal line is affected so that the normal part of the acoustic perturbation $u'_{ac,\perp}$ rises. The growth rate of the disturbance slows due to the smaller velocity u_2 in radial direction. Hence, the second and the third peak of the IR are damped compared to the lower confinement ratio. The oscillation frequency of the IR appears to be unaffected by the C_r variation. The timescale τ_r decreases with an increasing C_r. This can be explained by an increased bulk flow in x_1 direction.

Especially the influence of the gas expansion on the frequency of the oscillating IR is not fully understand yet and requires further investigation.

7.4 Relation to Known Physical Phenomena

To better understand the impact of the gas expansion on the FTF, this section draws a brief connection to well-known phenomena.

First, the mechanism that leads to the high peak in the IR is discussed. As shown in Figure 4.5, the normal acoustic velocity perturbation $u'_{ac,\perp}$ is high at the flame base and low at the flame tip. The high perturbation at the flame base then travels along the flame front and increases due to the Darrius-Landau mechanism [29]. This increase was also observed in the FTF modeled with the gas expansion effect. The IR with the gas expansion is higher than without it. Hence, the gas expansion is related to the Darrius-Landau mechanism. To further investigate this relation, a sinusoidal deflected flame front is analyzed. The flame front is located in a duct geometry and the modeled isoline represents the beginning of the flame front. The desingularized sources are therefore positioned in a distance r_0 behind the isoline, compare Section 5.2.2. For an unstretched flame front, the induced velocity u_{vol} towards that isoline vanishes, see Figure 5.6. The velocity field with the disturbed flame front is depicted in Figure 7.6. It can be seen that the gas expansion induces a negative axial velocity $u_{vol,1}$ at a convex (towards the unburnt gas) part of the flame front and a positive $u_{vol,1}$ at a concave part. This phenomena is less pronounced for a higher source radius r_0, compare Figure 7.6 (b). It is interesting to note that the Markstein number reduces the velocity differences along the flame front as well. The volume production scales with the burning velocity, which itself depends on Ma. A higher volume production is therefore expected at a concave part of the flame front. This variation in the volume production counteracts the induced velocity differences in the unburnt gas. However, for the investigated Markstein numbers the influence on u_{vol} is vanishingly small.

The second important effect that arises from the flame-flow feedback is the convective waves in the unburnt gas [2]. These waves dominate the motion of the unburnt fluid in the range of low Strouhal numbers f^* [2]. To analyze the impact of the gas expansion on the convective waves, a disturbed flame front isoline from the CFD simulations of Steinbacher et al. [26] is adopted. This isoline denotes the beginning of the flame front. The sources are once again positioned in a distance r_0 to that isoline, so that the velocity field u_{vol} is obtained. To extract the convective waves, the velocity field u_{ref} induced by an undisturbed flame shape is subtracted. Both, the modeled result with the gas expansion and the CFD simulation result are depicted in Figure 7.7. Even though the disturbance is not exactly the same in both pictures, it can be seen that the shape of the convective waves is similar. The magnitude of the waves corresponds reasonable well. In contrast to that a different phase of the waves can be observed. It is concluded that the gas expansion is linked to the convective waves, but especially the different phase arises questions.

Even though it was shown in this section that the gas expansion relates the Darrius-Landau mechanism and the convective waves, further investigation is required.

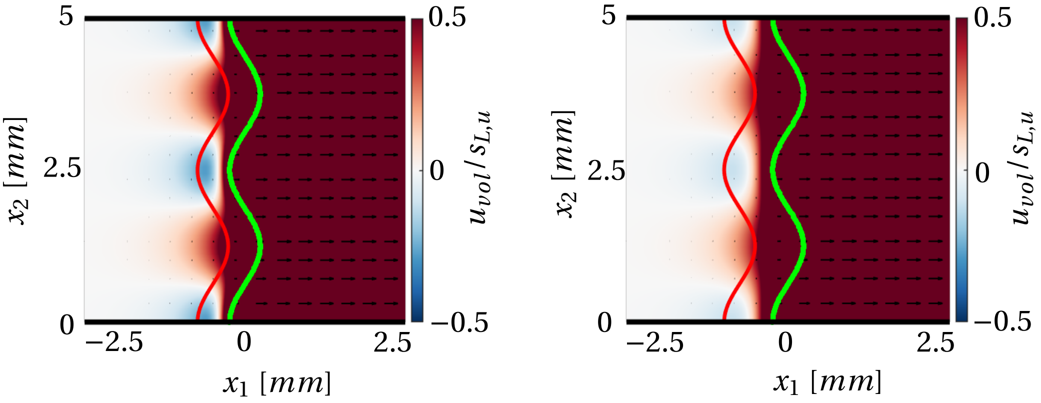

(a) (b)

Figure 7.6: Comparison of the gas expansion induced velocity field u_{vol} non-dimensionalized with the unburnt burning velocity $s_{L,u}$. The sources (—) are located in a distance r_0 behind the flame front (—). In (a) the source radius was chosen as $r_0 = 0.5[mm]$ and in (b) as $r_0 = 1[mm]$. Both results are obtained with the parameters: $E = 7$, $\delta_M = 1\ [mm]$.

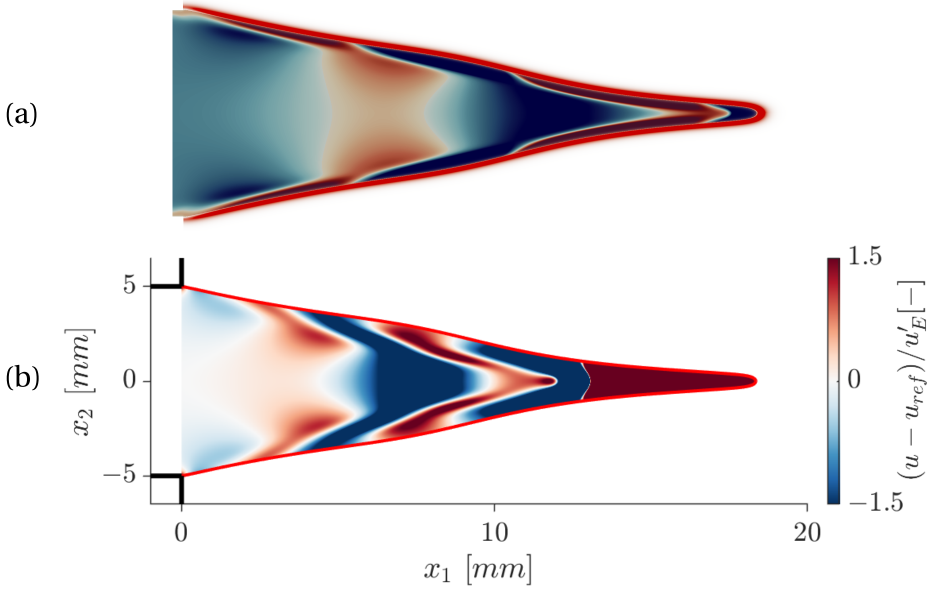

Figure 7.7: Comparison of the convective waves obtained by a CFD simulation from Steinbacher et al. [25] (a) and obtained by the modeled velocity field (b). The parameters used are: excitation velocity $u'_E = 0.02\ [m/s]$; $E = 7$; $s^0_{L,u} = 0.26\ [m/s]$. Graphic (a) is adopted from Steinbacher et al. [27].

8 Conclusion

The aim of this thesis was to develop a velocity model that can capture and characterize the impact of the gas expansion on the velocity field. This model should be fast to compute, but at the same time produce a realistic velocity field. The derived model was coupled with a G-equation solver from Steinbacher to investigate the influence of the gas expansion on the linear response of premixed flames.

To derive the new model, a new source was introduced. This source is based on the potential source, but distributes the volume production in space. In combination with conformal mappings, it was possible to evaluate the induced velocity field by this source in a duct geometry. By modeling several sources on the flame front, a continuous volume production along the flame front was obtained. This volume production then induced a velocity field. For an uncurved flame front, the impact on the unburnt gas vanished. However, the fluid through the flame front accelerated. By comparing the velocity profile through the unstretched flame front with the velocity profile from Cantera simulations, a very good alignment was detected. Hence, the task of an realistic velocity field is fulfilled. It was also explained that through the continuous velocity acceleration, several isolines in the flame front can be simulated with the G-equation solver. An investigation was conducted to find the optimal number of sources in order to produce an accurate simulation. It was concluded that $(4 \cdot L_f)/\delta_F$ sources are optimal for a simulation of an unstretched flame front. Hence, the task of an easy to compute velocity model is fulfilled.

By coupling the velocity model with the G-equation solver, an initial investigation of the impact of the gas expansion on the flame shape was conducted. It was determined that the gas expansion leads to a more curved flame front compared to the CFD simulation flame shapes. This corresponds well to the results of Choi and Shin [8]. Furthermore the impact of the flame thickness on the velocity field is captured by the derived model. It was found, that with an increasing flame thickness gradients in the velocity at the flame front decrease.

Afterwards, the impact on the FTF was investigated. It was found that the gas expansion has to be accounted for the swinging impulse response and the high magnitude in the frequency response.

At the end of this thesis it was shown that the gas expansion is linked to the convective waves and the Darrius-Landau mechanism and has to be accounted for both mechanisms.

For a quantitative statement towards the impact of the gas expansion on the flame shape and the FTF, further investigation is required to determine the uncertain value of the Markstein number. It would also be interesting to combine the derived model for the gas expansion with the shear layer model of Blanchard et al. [3] to investigate the interaction of barocline vorticity and the gas expansion.

Bibliography

[1] D. Adalsteinsson and J. A. Sethian. The Fast Construction of Extension Velocities in Level Set Methods. *Journal of Computational Physics*, 148(1):2–22, 1999.

[2] A.L. Birbaud, D. Durox, and S. Candel. Upstream flow dynamics of a laminar premixed conical flame submitted to acoustic modulations. *Combustion and Flame*, 146(3):541–552, aug 2006.

[3] M. Blanchard, T. Schuller, D. Sipp, and P. J. Schmid. Response analysis of a laminar premixed M-flame to flow perturbations using a linearized compressible Navier-Stokes solver. *Physics of Fluids*, 27(4):43602, apr 2015.

[4] R. S. Blumenthal, P. Subramanian, R.I. Sujith, and W. Polifke. Novel perspectives on the dynamics of premixed flames. *Combustion and Flame*, 160(7):1215–1224, jul 2013.

[5] D. Bradley, M. Lawes, K. Liu, S. Verhelst, and R. Woolley. Laminar burning velocities of lean hydrogen–air mixtures at pressures up to 1.0 MPa. *Combustion and Flame*, 149(1):162–172, 2007.

[6] M. Brandl. Simulation of Self Sustained Thermoacoustic Oscillations by Coupling of a Low-Order Acoustic Network Model with a Level-Set Solver, 2016.

[7] J. W. Brown and R.V. Churchill. *Complex Variable and Applications*. McGraw-Hill Higher Education, 8 edition, 2009.

[8] B. I. Choi and H. D. Shin. Flame/Flow Interaction in Oscillating Flow Field. *Combustion Science and Technology*, 159(1):87–107, oct 2000.

[9] B.-T. Chu and L. S. G. Kovásznay. Non-linear interactions in a viscous heat-conducting compressible gas. *Journal of Fluid Mechanics*, 3(05):494, feb 1958.

[10] P. Clavin and J. C. Graña-Otero. Curved and stretched flames: the two Markstein numbers. *Journal of Fluid Mechanics*, 686:187–217, 2011.

[11] A. Cuquel, D. Durox, and T. Schuller. Theoretical and experimental determination of the transfer function of confined premixed conical flames. *Proceedings of the Combustion Institute*, 34:1007–1014, 2013.

[12] M. Fleifil, A. M. Annaswamy, Z. A. Ghoneim, and A. F. Ghoniem. Response of a laminar premixed flame to flow oscillations: A kinematic model and thermoacoustic instability results. *Combustion and Flame*, 106(4):487–510, 1996.

[13] J. J. Keller. Thermoacoustic oscillations in combustion chambers of gas turbines. *AIAA Journal*, 33(12):2280–2287, dec 1995.

[14] A. R. Kerstein, W. T. Ashurst, and W. A. Forman. Field equation for interface propagation in an unsteady homogeneous flow field. *The American Physical Society*, 37(7), 1988.

[15] T. Lieuwen. Modeling Premixed Combustion-Acoustic Wave Interactions: A Review. *Journal of Propulsion and Power*, 19(5):765–781, sep 2003.

[16] T. Lieuwen. Unsteady Combustor Physics. Cambridge University Press, New York, UNITED STATES, 2012.

[17] S. J. Osher and J. A. Sethian. Fronts Propagating with Curvature Dependent Speed. *Computational Physics*, 79(1):1–5, 1988.

[18] H. Pitsch. Laminar Premixed Flames : Kinematics and Burning Velocity. In *CEFRC Combustion Summer School*, 2014.

[19] C. W. Rhee. Evolution of flame shape to a vortex pair. *KSME International Journal*, 15(5):623–629, 2001.

[20] K. Satheesh, G. Srinivas, and S. Hemchandra. An advection velocity correction scheme for interface tracking using the level-set method. *Computers and Fluids*, 168:232–244, 2018.

[21] S. Schlimpert, S. Hemchandra, M. Meinke, and W. Schröder. Hydrodynamic instability and shear layer effect on the response of an acoustically excited laminar premixed flame. *Combustion and Flame*, 162(2):345–367, feb 2015.

[22] T. Schuller, D. Durox, and S. Candel. A unified model for the prediction of laminar flame transfer functions: Comparisons between conical and V-flame dynamics. *Combustion and Flame*, 134(1-2):21–34, jul 2003.

[23] T. Steinbacher. personal correspondence. *steinbacher@tfd.mw.tum.de*.

[24] T. Steinbacher. GFlame. Sofware, Professur für Thermofluiddynamik, TUM Garching. *steinbacher@tfd.mw.tum.de*, aug 2018.

[25] T. Steinbacher, A. Albayrak, A. Ghani, and W. Polifke. Consequences of Flame Geometry for the Acoustic Response of Premixed Flames. *submitted to Proceedings of the Combustion Institute.*

[26] T. Steinbacher, A. Albayrak, A. Ghani, and W. Polifke. Response of premixed flames to irrotational and vortical velocity fields generated by acoustic perturbations. *Proceedings of the Combustion Institute*, aug 2018.

[27] T. Steinbacher, A. Albayrak, A. Ghani, and W. Polifke. Response of premixed flames to irrotational and vortical velocity fields generated by acoustic perturbations. *37th International Symposium and Combustion*, aug 2018.

[28] M. Sussman, P. Smereka, and S. Osher. A Level Set Approach for Computing Solutions to Incompressible Two-Phase Flow, 1994.

[29] J.-M. Truffaut and G. Searby. Experimental Study of the Darrieus-Landau instability on an inverted-'V' flame, and measurement of the Markstein number. *Combustion Science and Technology*, 149(1-6):35–52, dec 1999.